Comparison of Propeller-Wing Interaction Simulation using Different Levels of Fidelity

Zhi Yang [*]

Scientific Simulations LLC, Laramie WY

Andrew C. Kirby [†]   Dimitri J. Mavriplis [‡]

University of Wyoming, Laramie WY

Low fidelity and high fidelity computational fluid dynamic models are applied to the propeller-wing configuration of the Workshop for Integrated Propeller Prediction (WIPP) using an unstructured mesh solver: a steady-state Reynolds-averaged Navier-Stokes (RANS) approach with an actuator disk model, an unsteady RANS approach with overset blade resolved meshes, and a hybrid RANS-LES approach with overset blade-resolved meshes and an adaptively refined background mesh. Results between the three methods are analyzed and compared to experimental data provided by the workshop.

I.   Introduction

Since the first flight by the Wright brothers more than one hundred years ago, propeller-driven aircraft have been a major research area in aeronautics. In recent years, a resurgence of propeller-driven aircraft research has occurred due to a growing interest in electric vertical takeoff and landing aircraft (eVTOL), UAV/MAV (Micro Aerial Vehicle), PAV (Personal Aerial Vehicle), and electric propulsion. With increasing computational capability, computational fluid dynamics (CFD) has become a powerful tool for aerodynamic analysis and design. Accurate modeling of the propellers is challenging due to flow interaction caused by the rotational motion of the blades with respect to the wing and fuselage. This renewed interest in propeller-driven aircraft creates the need for CFD validation, given the limited availability of propeller test data.

An open test database of wing and propeller interactions for CFD validation was completed recently by Helden Aerospace and ESAero,[1] conducted in the Lockheed Martin Low-Speed Wind Tunnel (LSWT). The wind tunnel model included a tip-mounted 10% scale C-130H four-bladed propeller and a semi-span wing similar in geometry to the NASA X-57 experimental aircraft. The geometry model used for the experiment is shown in Figure 1 and summarized as follows:[2]

- Number of Blades: 4

- Blade Radius: $R = 8.1$ [in]

- Reference Area: 675.6 [in]^2

- Propeller Center: $(-1.15, 67.45, 0.0)$ [in]

- $Re = 0.5678 \times 10^6$ with a reference length 1 [ft]

The test model wing is mounted on a standoff device and the wing force balance data is obtained for all flow conditions with six integrated sections of pressure taps, as shown in Figure 2. The experiment conducted several cases for detailing wing and propeller performance varying flow speed, angle of attack, and thrust coefficient. Pressure distribution measurements on the wing and the wake flow of the propeller were collected. Additionally, a wake survey was conducted for the zero degree angle of attack case, profiling the axial, radial, and tangential flow velocities at multiple downstream locations from the propeller.

---

[*]Research Scientist, AIAA member; email: zyang@scientific-sims.com

[†]Research Scientist, AIAA member; email: akirby@uwyo.edu

[‡]Professor, AIAA Associate Fellow; email: mavriplis@uwyo.edu

American Institute of Aeronautics and Astronautics

In this paper, we investigate the propeller-driven flow by using three levels of simulation fidelity: a steady-state Reynolds Averaged Navier-Stokes (RANS) solver with actuator disk model, an unsteady RANS model with blade and wing overset meshes, and an unsteady hybrid RANS-LES (Large Eddy Simulation) model with overset meshes. In the following sections, we first outline the flow solvers and the computational methodology used herein. This is followed by a presentation and comparison of the results using all three methods. Conclusions are drawn based on the observed accuracy and expense of the various simulations approaches.

II. Computational Methodology

The low-fidelity model utilizes an actuator-disk approach coupled to a finite-volume Reynolds-averaged Navier-Stokes (RANS) solver on unstructured mixed-element meshes and is solved as a steady-state problem. The mid- and high-fidelity models utilize an overset mesh paradigm involving multiple independent overlapping meshes, with the global solution established by an overset grid assembler. All meshes are solved using the RANS solver in time-dependent mode in the mid-fidelity model. In contrast, the high-fidelity model employs a second flow solver on an additional background wake mesh based on the Large Eddy Simulation formulation. We detail the flow solvers, actuator disk model, and the overset mesh paradigm in the following subsections.

A. Reynolds-Averaged Navier-Stokes Solver

The aerodynamic analysis capability for this work is based on the NSU3D unstructured mesh RANS CFD solver.[3] The Navier-Stokes equations in conservative form can be written as:

$$\frac{\partial \mathbf{U}}{\partial t} + \nabla.(\mathbf{F}(\mathbf{U}) + \mathbf{G}(\mathbf{U})) + \mathbf{S} = \mathbf{0} \tag{1}$$

where $\mathbf{U}$ represents the vector of conserved quantities (mass, momentum, and energy), $\mathbf{F}(\mathbf{U})$ represents the convective fluxes, $\mathbf{G}(\mathbf{U})$ represents the viscous fluxes and $\mathbf{S}$ represents additional source terms, which may be introduced by the actuator disk model.

NSU3D is a modular compressible Reynolds-averaged Navier–Stokes (RANS) CFD solver for unstructured meshes, including an actuator disk model, which can be used to investigate propeller-driven flow as a low-fidelity model. It also includes a dynamic overset mesh interface capability for high-fidelity time-accurate simulations for geometries with relative component motion, such as rotating blades in the presence of a wing or fuselage.

For the current simulations, NSU3D operates on unstructured hybrid meshes using prismatic elements in boundary layer regions and tetrahedral meshes in outer regions with small numbers of pyramidal elements occurring at the edge of boundary layer regions. The discretization is based on a finite-volume approach with matrix-based artificial dissipation which is nominally second-order accurate. The current work uses the Spalart-Allmaras (SA) turbulence model following the implementation devised for avoiding negative eddy viscosity values, as described in reference.[4] The basic solver employs a line-implicit method, which is used as a smoother on fine and coarse levels of an agglomeration multigrid solver.[5] This basic solver strategy can be employed directly as an iterative nonlinear solver, or as a linear preconditioner for use in a Newton-Krylov method. NSU3D has been well validated for low-speed and transonic cruise problems as a regular participant in the AIAA High Lift Prediction Workshop (HLPW) series[6] and the Drag Prediction Workshop (DPW) series.[7] NSU3D is employed on all unstructured meshes throughout this work.

B. Large Eddy Simulation Solver

In the high-fidelity model, a Large Eddy Simulation (LES) solver is introduced for resolving the off-body regions of the flow, particularly the wake region. The solver used herein is dg4est[8,9] which is a combination of the nodal Discontinuous Galerkin (DG) solver CartDG[10–12] coupled with the dynamic adaptive mesh refinement framework p4est.[13] The numerical kernel, CartDG, discretizes the compressible Navier–Stokes equations and implements the constant Smagorinsky Subgrid-Scale (SGS) model for turbulence.[14] To achieve high computational efficiency, CartDG exploits simplifications in Cartesian mesh settings and utilizes a tensor-product, collocation-based DG method. To improve the numerical stability of the DG method, CartDG's formulation is based on a split-form flux scheme possessing the summation-by-parts property to mimic integration-by-parts discretely.[15] In the context of dynamic overset grid simulations paired with NSU3D as a near body solver, dg4est has been validated on wind energy[16–18] and rotorcraft[19] applications.

American Institute of Aeronautics and Astronautics

DIMENSION	VALUE
PLANFORM AREA (IN.^2)	675.6
ASPECT RATIO	6.7
TAPER RATIO	0.7
ROOT CHORD (IN.)	11.6
TIP CHORD (IN.)	8.6
MAC (IN.)	10.15
LEADING EDGE SWEEP (DEG.)	1.9
WING SCALE (% OF X-57)	40.5
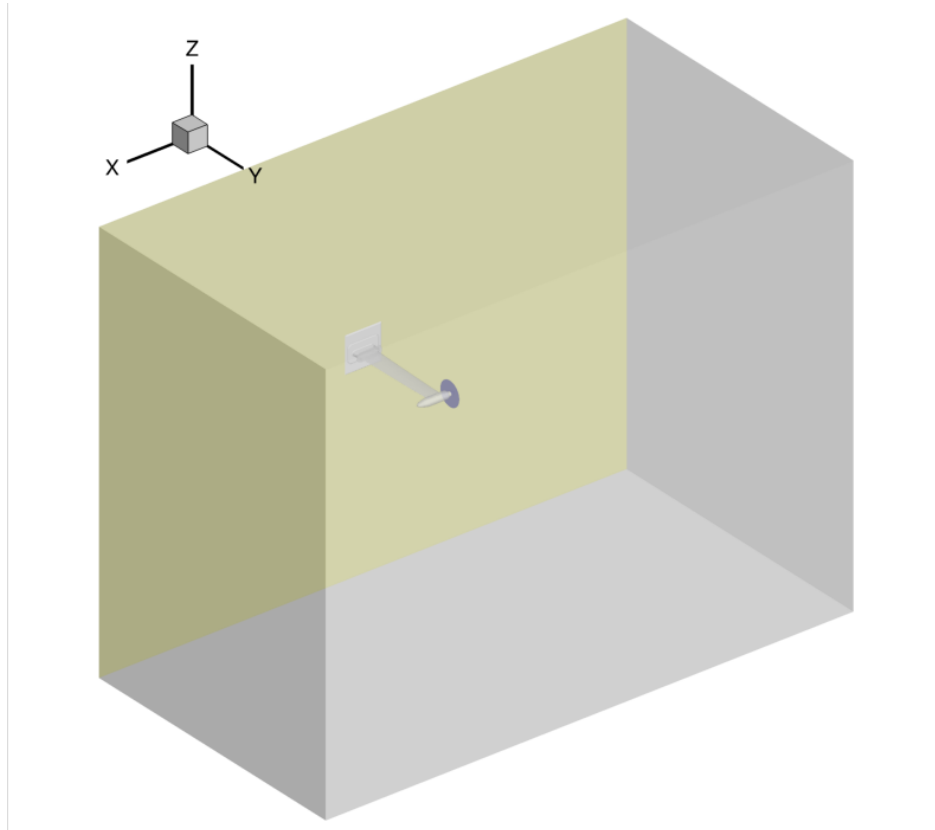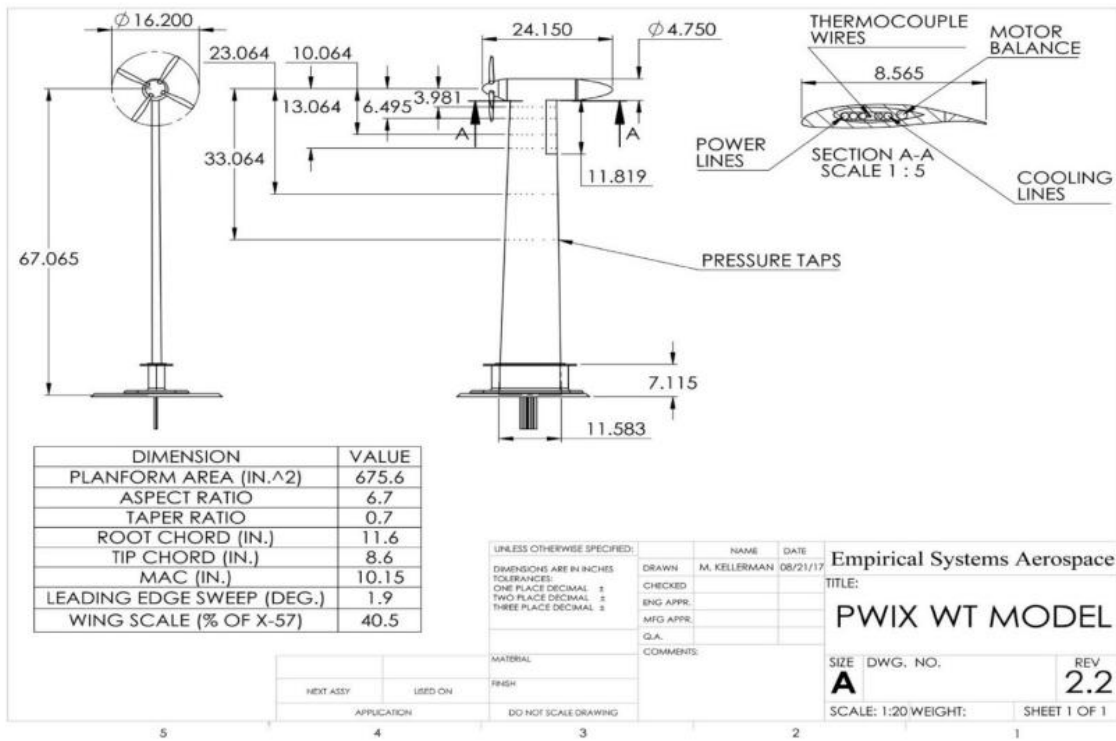
Figure 1: Geometry description reproduced from reference[2] (upper) and geometry model (lower) used for computations.

American Institute of Aeronautics and Astronautics
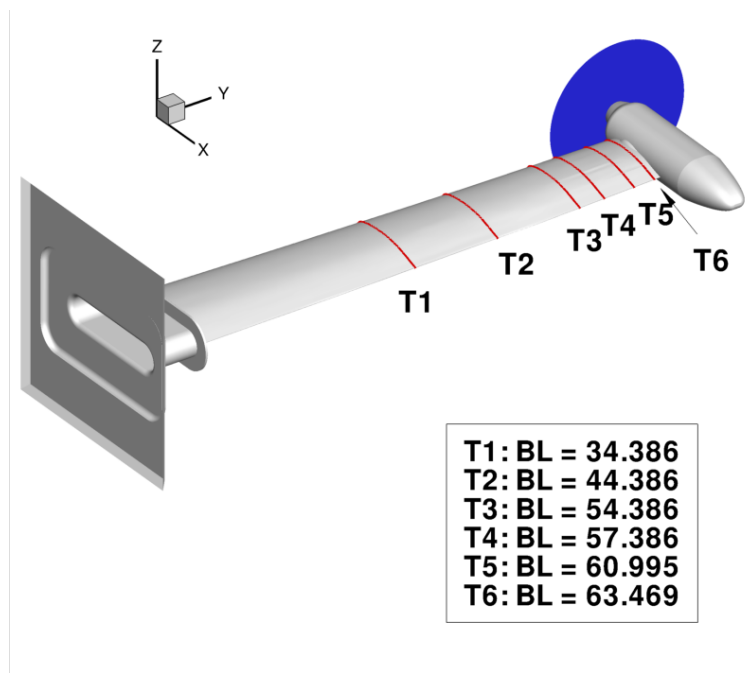
Figure 2: Pressure tap locations (T1–T6) on wing.

C. Actuator Disk

The actuator disk model is a low-fidelity method for analyzing the performance of a propeller or rotor[20] and is implemented in NSU3D for this work. In this method, the propeller or rotor is represented by a disk (without thickness) or a cylinder (with thickness),[21] which is subject to the influence of the blades but allows the flow to pass through the propeller or rotor. Based on the conservation of mass, momentum and energy, the influences of the blades are distributed as source terms on the disk or cylinder. The source terms can be written as:[20]

$$S = \begin{Bmatrix} 0 \\ f_x \\ f_y \\ f_z \\ f_x u + f_y v + f_z w \end{Bmatrix} \tag{2}$$

where fx, fy, and fz are the momentum sources resulting from the force components on the rotor in the x, y, and z directions, respectively and u, v, and w are the flowfield velocity components. A two-dimensional structured grid for the actuator disk or a three-dimensional structured grid for the actuator cylinder is created automatically using input parameters and inserted into the unstructured volume grid. The sources are then associated with the nearest node in the unstructured volume grid and added to the system of equations at the associated node's control volume. Because no physical blade geometry is simulated, the influence of the rotor is enforced by the aerodynamic loading model in the actuator disk method. Therefore, the aerodynamic loading model plays a critical role in the actuator disk method.

Three types of load models are possible:[20]

- Assumed distribution: For a given thrust coefficient C_T and power coefficient C_Q, the loading can be obtained by assuming a prescribed disk load distribution, such as a linear distribution in the radial direction.

- Prescribed loading (AD): The loading is given by other methods or by test data, which is the approach used in this paper. Here, the thrust/torque distribution along the radial direction was provided by the workshop organizers. The loading distributions are shown in Figure 3, which is reproduced from workshop provided data, obtained from wake survey measurements. The different series in the figure correspond to different thrust

American Institute of Aeronautics and Astronautics

coefficients and freestream conditions, as defined in Table 1. Here, loading parameters are defined as:

$$CTRDR = \rho_\infty U \left(U - U_\infty \right) \left(r/R \right) / Q_\infty \tag{3}$$

$$CQRDR = \rho_\infty U V_{swirl} \left(r/R \right)^2 / Q_\infty \tag{4}$$

where ρ_∞ is the freestream fluid density, U_∞ is the freestream velocity, U is the measured local axial velocity, V_{swirl} is the measured local swirl velocity, Q_∞ represents the dynamic pressure, and r/R denotes the radial position along the disk or blade span.

- Blade-element (BE) theory loading: If the blade geometry is known, the blade-element method can be applied to compute the loading for the actuator disk. Local flow properties such as Mach number and flow direction can be obtained at any location on the actuator disk from the CFD flow solution. The flow direction combined with the blade geometry and rotational speed can be used to obtain the effective local angle of attack. With the local Mach number and the effective angle of attack, the lift/drag coefficients can be obtained from sectional airfoil CL/CD-AoA-Ma tables or charts and used to prescribe the appropriate momentum source terms as described by equation (2). In this work, blade-element actuator disk runs were also performed. Seven sectional airfoil geometries were obtained by taking cross-sectional cuts of the blade mesh described in the subsequent section. Two-dimensional airfoil lift and drag curves were obtained using the NSU2D RANS code[22] (the two-dimensional counterpart to the NSU3D code) at various Mach numbers, resulting in airfoil performance curves to be used by the blade-element actuator disk, as shown in Figure 4. Here the airfoils denoted s1 to s7 correspond to airfoils extracted from root to tip along the blade span.

RUN	Ma	C_T	N [rev/sec]	V [ft/sec]	RHO [slug/ft³]	
79 180	0.08	0.4	98.42	92.77	0.0023	Series 2
87	0.08	0.2	78.41	90.52	0.0024	Series 5
84	0.08	0.04	57.60	90.63	0.0024	Series 8

Table 1: Description of various WIPP experimental data sets as detailed in references[1, 2]
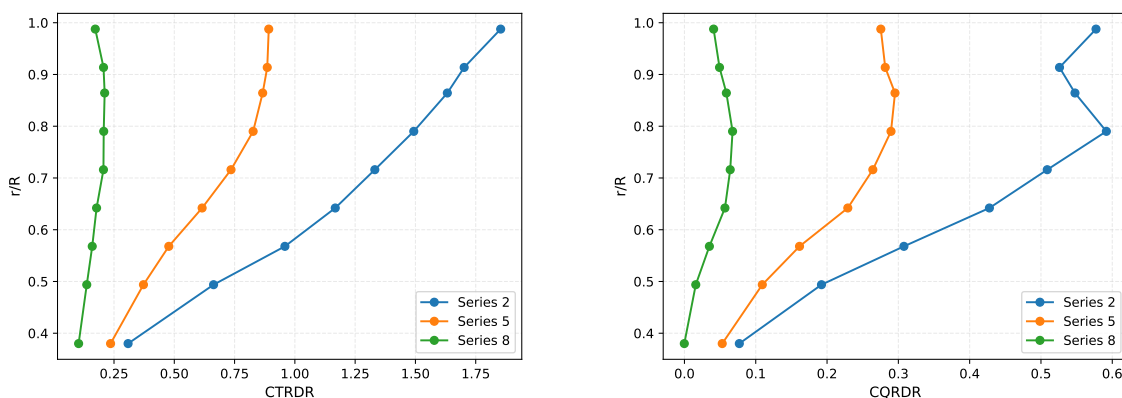

Figure 3: Propeller radial thrust distribution (left) and torque distribution (right) as specified by workshop data.

D. Mesh, Solver, and Overset Configurations

Different meshing, oversetting and solver configurations are employed for the different levels of simulation fidelity. The lowest fidelity approach employs a single unstructured mesh paired with the actuator disk model using either user-input loading data (i.e. as prescribed by Figure 3) or the loading produced by the blade-element theory (i.e. obtained from airfoil properties in Figure 4). Alternatively, the mid-fidelity approach employs five unstructured meshes, consisting of four moving blade meshes overset with the global wing-body mesh which fills the computational

American Institute of Aeronautics and Astronautics
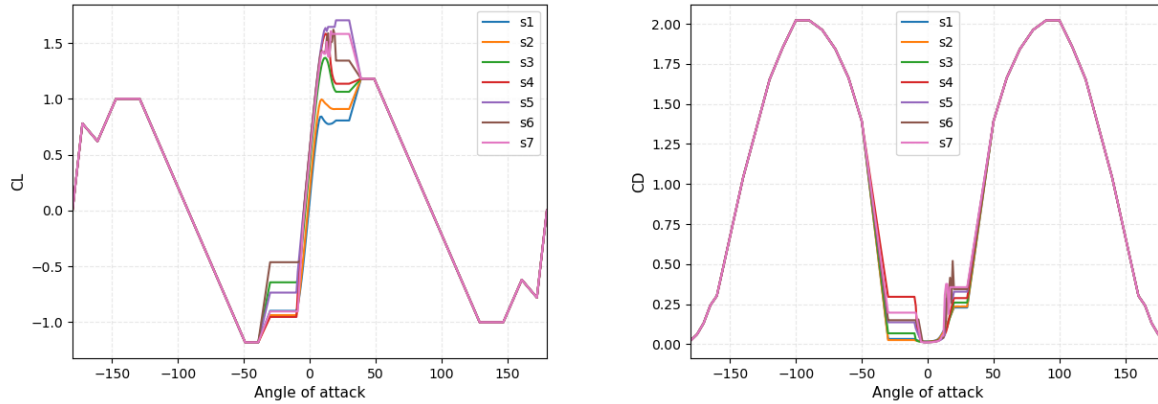
Figure 4: Force coefficient tables computed using 2D RANS code (NSU2D) at Mach=0.4 used for the blade-element (BE) actuator-disk loading for different sectional airfoils along the span of the propeller blade going from root (s1) to tip (s7).

domain. The highest fidelity approach employs six meshes: four unstructured blade meshes, a single unstructured wing-body mesh that only extends a small distance away from the body, and a background dynamically adaptive Cartesian mesh which covers the entire computational domain. For the low- and mid-fidelity modes, the RANS NSU3D solver is used exclusively, in steady-state mode for the former, and time-dependent mode for the latter. In the high-fidelity model, the RANS NSU3D code is employed for the unstructured meshes in time-dependent mode, and the LES flow solver `dg4est` is used on the adapting Cartesian mesh.

For the mid and high-fidelity models, the dynamic overset mesh approach is used for simulating bodies in relative motion such as the flow field of a propeller or rotor near a static wing. This approach allows multiple meshes, and optionally, multiple flow solvers. Herein, the data exchange between the moving blade mesh blocks and the static background mesh block is handled by TIOGA[23, 24] (Topology Independent Overset Grid Assembler). The TIOGA overset grid assembler relies on an efficient parallel implementation of Alternating Digital Trees (ADT) for point-cell inclusion testing in order to determine the interpolation patterns between overlapping meshes. Multiple mesh blocks are loaded in parallel and TIOGA computes the cell donor-receptor information required by the flow solver. The donor-receptor information is saved in an array called `IBLANK`, which assigns three possible values: -1 (fringe), 0 (hole), 1 (field). A hole cell occurs when a mesh block overlaps another mesh block and falls within an enclosed surface, such as the interior of a blade. Fringe cells are tagged for transferring data between overset meshes, whereby a given cell's data is interpolated from other meshes overlapping its extents. Lastly, field cells represent valid data cells and are determined either as cells in regions with no overlap, or cells in regions of overlap that have the highest local resolution compared to the other overlapping component mesh cells.

1. Low-fidelity Model

The low-fidelity model uses an unstructured mesh approach to discretize the static wing body, which contains the entire computational domain including the wing, nacelle, standoff, and wake region. Two unstructured meshes are used in this work and were provided upon request by the WIPP workshop organizers. The first unstructured mesh used for the low-fidelity model is the workshop mesh PWIX_DSV2_AIL0_AD_F_FUN3D, shown in Figure 5 labeled herein as (AD1.0), containing approximately 5.4 million nodes, 7.5 million prisms, 70,000 pyramids, and 9 million tetrahedra. This mesh contains a zero thickness surface that conforms to the actuator disk, with additional refinement at the disk location as shown in the left subfigure of Figure 6. The other mesh utilized for the low-fidelity model is the PWIX_DSV2_AIL0_NP_F_R0p70_FUN3D, labeled herein as NP0.7, which corresponds to the mesh used for the FUN3D simulations in reference.[25] Mesh NP0.7 includes approximately 15 million nodes, 26 million prisms, 130,000 pyramids, and 12 million tetrahedra. As the low-fidelity model is based on an actuator disk approach, no additional unstructured mesh is used to directly discretize the propeller blades. As mentioned previously, a virtual disk surface (or cylinder) is generated internally by the actuator disk software and used to place the momentum sources. However, this disk does not conform to the unstructured mesh topology, and the distributed disk sources are automatically

American Institute of Aeronautics and Astronautics

interpolated onto the unstructured mesh at run time. The actuator disk runs are performed on both unstructured meshes in order to examine the effect of the presence of a conforming disk surface and associated refinement on the overall solution accuracy.

2. Mid-fidelity Model

The mesh utilized for the mid-fidelity model is the PWIX_DSV2_AIL0_NP_F_R0p70_FUN3D mesh NP0.7, which corresponds to the second mesh used in the low-fidelity model. Additionally, the mid- and high-fidelity models use overset-type simulations, where the propeller blades are discretized with a separate unstructured mesh, replicated four times times to account for all four blades. The blade mesh used in this work was kindly provided by the authors of reference.[25] The mesh contains approximately 0.82 million nodes, 0.82 million tetrahedra, 7,000 pyramids and 1.3 million prisms. The right subfigure of Figure 6 shows the blade meshes used in the higher-fidelity models. As discussed in reference,[25] the blade mesh was based on a geometry reconstructed from the laser scan of the blade provided by the workshop organizers. Two modifications to the blade geometry were performed in reference[25] in order to produce a suitable grid. Firstly, the leading edge was modified using a fillet to obtain a smoother profile, and secondly a small portion of the blade span near the root was deleted in order to introduce a gap between the blades and the spinner, which facilitates varying the blade pitch within the overset mesh framework. More details on these modifications and their potential effect on the overall simulation results can be found in reference.[25]
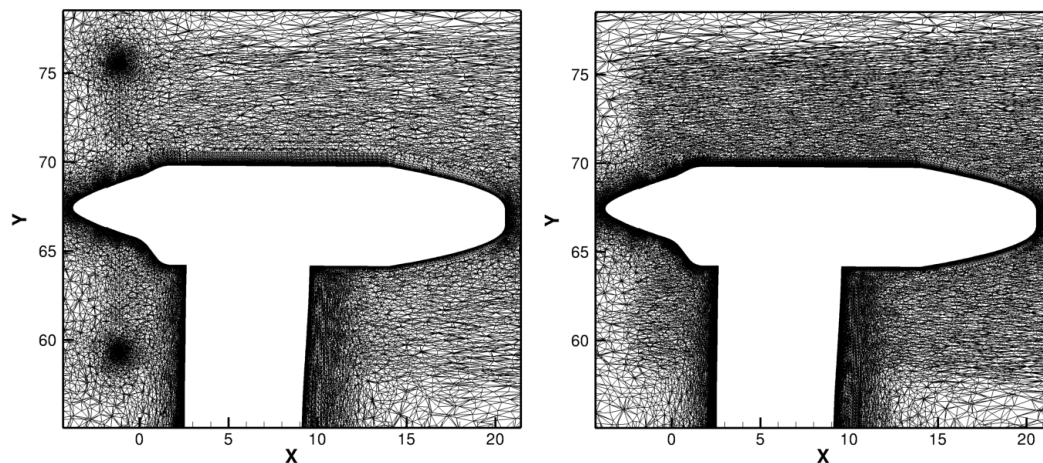

Figure 5: Mesh slice at $z = 0$ for mesh AD1.0 (left) and mesh NP0.7 (right).
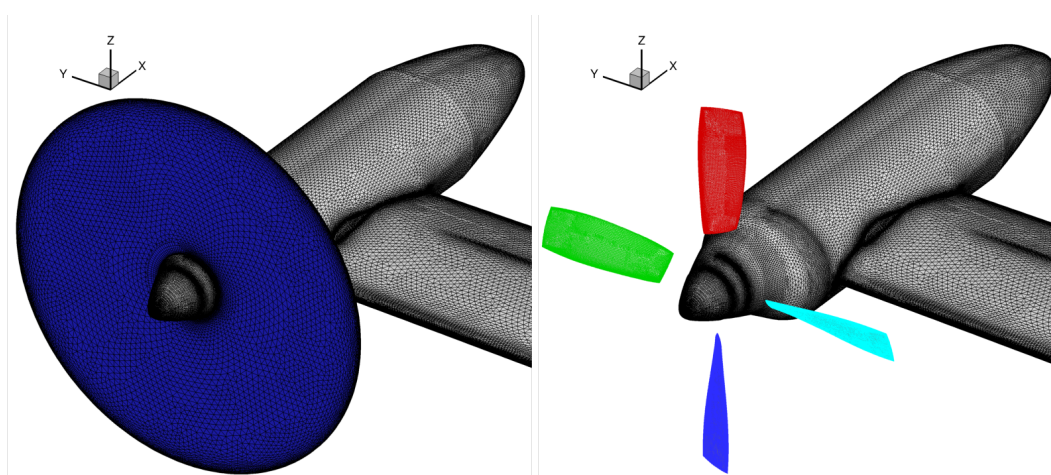
Figure 6: (left) Surface mesh near the wing tip-nacelle for mesh AD1.0 showing zero thickness disk and (right) for mesh NP0.7 with blade meshes included (right)

American Institute of Aeronautics and Astronautics

The blade meshes are overset with one or more background meshes. For the mid-fidelity model, the NP0.7 unstructured wing-body mesh described above serves as the sole background mesh, which is responsible for discretizing the complex wing-body geometry and wake regions. In contrast to mesh AD1.0, mesh NP0.7 does not contain any special treatment in the region of the actuator disk. However, this mesh contains moderate refinement behind the blades and nacelle in the wake regions.

As mentioned previously, in regions of mesh overlap, the overset mesh paradigm automatically chooses the component mesh cells with the highest resolution as the dominant component. Nevertheless, the extent of the flow domain swept out by the blade mesh can affect the overall solution results due to differing overset mesh interpolation patterns. The NSU3D software includes a facility for trimming back or cutting component meshes based on distance from the wall. In this facility, all cells further from the body than the user prescribed cut-distance are discarded for the overset mesh simulations. For the mid-fidelity model using overset blade meshes, a comparison of the mesh-cut distances on the blades is performed. Three cut-distance scenarios are tested and labelled as: No-Cut, Cut-2.5, and Close-Cut. The No-Cut scenario uses the entire component blade mesh, which extends approximately 4 inches out from the blade surface. For the Cut-2.5 scenario, the blade mesh is trimmed back to 2.5 inches, and for the Close-Cut, the blade mesh is cut off 1.0 inch from the blade surface. Figure 7 and 8 show the z-direction slices and x-direction slices, respectively, overset with the off-body unstructured mesh NP0.7. The IBLANK patterns are illustrated on the near-body blade meshes and the background mesh. The impact of the extent of the overset blade mesh on the predicted aerodynamic quantities is analyzed in the results section.

3. High-fidelity Model

In contrast to the mid-fidelity model, the high-fidelity approach utilizes multiple background meshes to cover the wing-body and the wake region. First, the Close-Cut blade meshes are selected for this model and overset with the NP0.7 near-body wing-nacelle mesh, which is trimmed to a fixed distance of 2.0 inches from the body surfaces. Then an adaptive Cartesian mesh is overlaid on the wing body forming the remainder of the computational domain and resolving the wake flow structures as show in Figure 9. Furthermore, the LES solver dg4est is employed on this Cartesian mesh using an *hp*-Discontinuous Galerkin (DG) formulation. In the regions of overlap with the blade and wing-body meshes, the off-body Cartesian mesh is refined to eight levels resulting in a spatial resolution of 0.15625 inches, and a prescribed second-order, $p = 1$, polynomial solution order is used for the DG solver. This approach has been found to be necessary in order to match both resolution and solution discretization order in the overlap regions between the DG off-body solver and the finite-volume near-body solver. The mesh refinement algorithm only allows for 2:1 coarsening between neighboring cells, thus a gradual coarsening occurs from the refined overlap regions to the off-body regions of the mesh. At startup, the far-field and wake regions are discretized by coarse 20-inch isotropic Cartersian cells, using a $p = 5$ (sixth-order accurate) DG discretization. As the time-dependent solution proceeds, the wake region is refined by the dynamic adaptive mesh algorithm, driven by a feature-based vorticity magnitude threshold applied periodically at every 10 global time steps. A total of six levels of refinement are permitted in the adaptive mesh refinement algorithm, while maintaining a 2:1 refinement between adjacent cells, and using six-order, $p = 5$ DG discretization except in the vicinity of the near-body meshes where the discretization is reduced gradually to $p = 1$, using an intermediate layer of $p = 3$ cells.

III.   Results and Analysis

Several of the data sets used for CFD comparison in the WIPP workshop are shown in Table 1. RUN79, RUN87, and RUN84 constitute the propeller wake survey, and RUN180 assesses the wing performance impact over a range of flow incidences. In this work, we present results for RUN79 and RUN180. For all cases, low fidelity (i.e. steady-state actuator disk), mid-fidelity (i.e. overset RANS) and high-fidelity (i.e. overset adaptive RANS-LES) simulations were performed. Furthermore, for the low-fidelity cases, two meshes (AD1.0 and NP0.7) were used, and two actuator disk methods (prescribed loading and blade-element loading) were run. For the mid-fidelity runs, three blade mesh-cut extents were examined, while the high-fidelity runs used only the close-cut blade mesh. The low-fidelity simulations were run as steady-state RANS problems, while the blade resolved simulations were run as time-dependent problems using a 0.5 degree blade revolution time step and a 0.25 blade time step for the mid-fidelity and high-fidelity methods, respectively. In all the presented results, the actuator disk results are taken as the final steady-state results of the simulation, while the blade-resolved simulations employed averaging of the computed values over one quarter of a propeller revolution for the mid-fidelity RANS results and 1.5 revolutions for the high-fidelity RANS-LES results, where the solutions are sampled at one degree propeller rotation intervals.
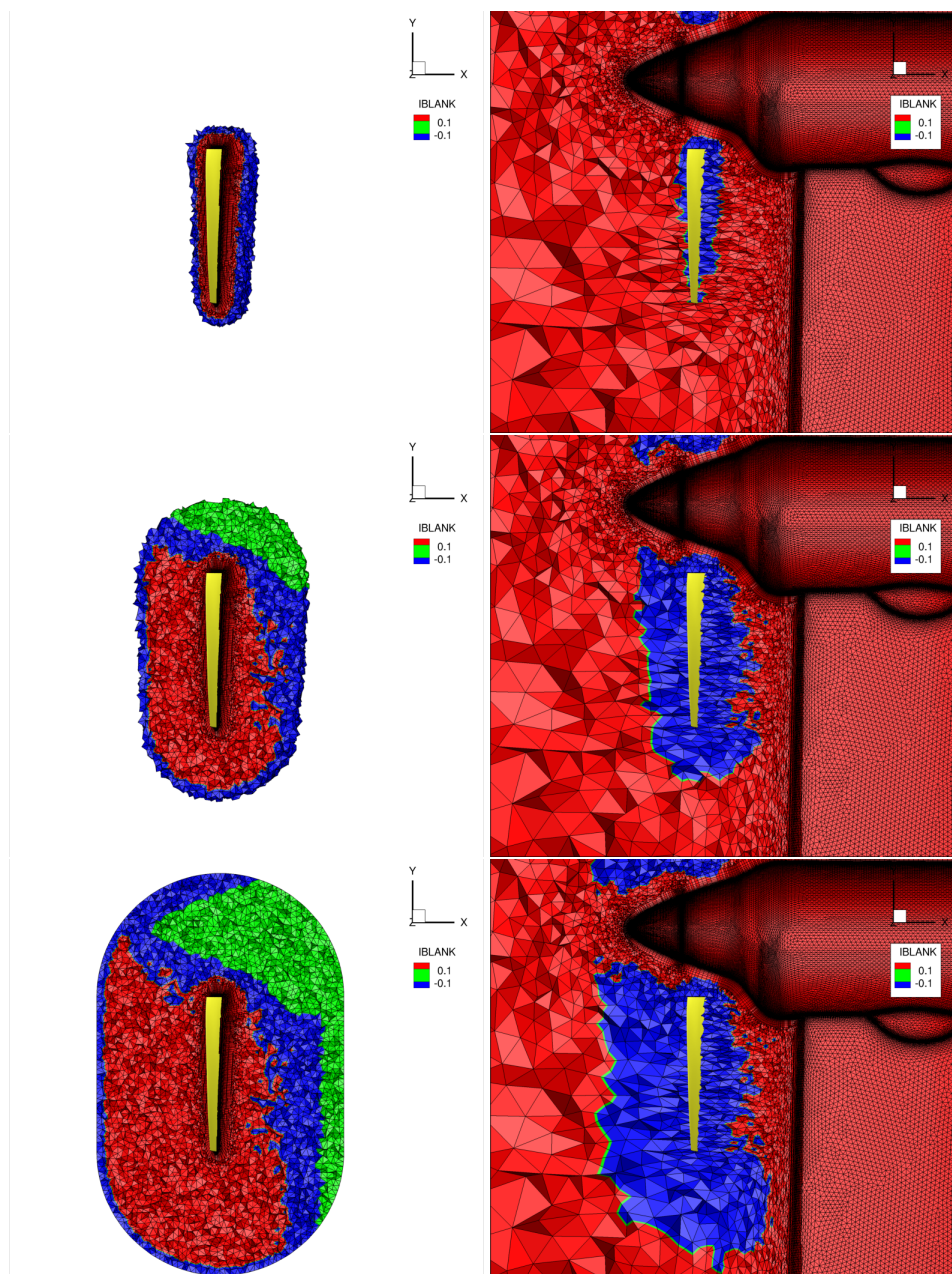
Figure 7: Mesh slices at $z = 0$ for overset mesh Close-Cut (upper), Cut-2.5 (middle) and No-Cut (bottom). Red indicates valid mesh cells, blue indicates fringe mesh cells (interpolated values), and green indicates hole mesh cells.

A.   RUN180 Results

Figure 10 shows the lift curve and drag polar with thrust included compared between test data and all simulations for RUN180 with $Ma = 0.08$, $C_t = 0.4$ across multiple angles of attack. The lift coefficients at low angles of attack closely track the experimental data but begin to overshoot beyond seven degrees. From the drag polar figure, the simulations are seen to generally under-predict drag, particularly at lower lift conditions. Comparing the two meshes (AD1.0 and NP0.7) using the prescribed disk loading, similar lift and drag values are observed at lower angles of attack. However, at the highest angles of attack, the AD1.0 mesh results produce lower C_L values which are closer to the experimental values. This indicates that additional mesh refinement in the vicinity of the actuator disk, as can be found in mesh AD1.0 (see Figure 5), may improve solution accuracy. Comparing the two actuator disk loading approaches, i.e. the prescribed loading provided by the workshop organizers based on wake surveys versus the blade-element loading,

American Institute of Aeronautics and Astronautics
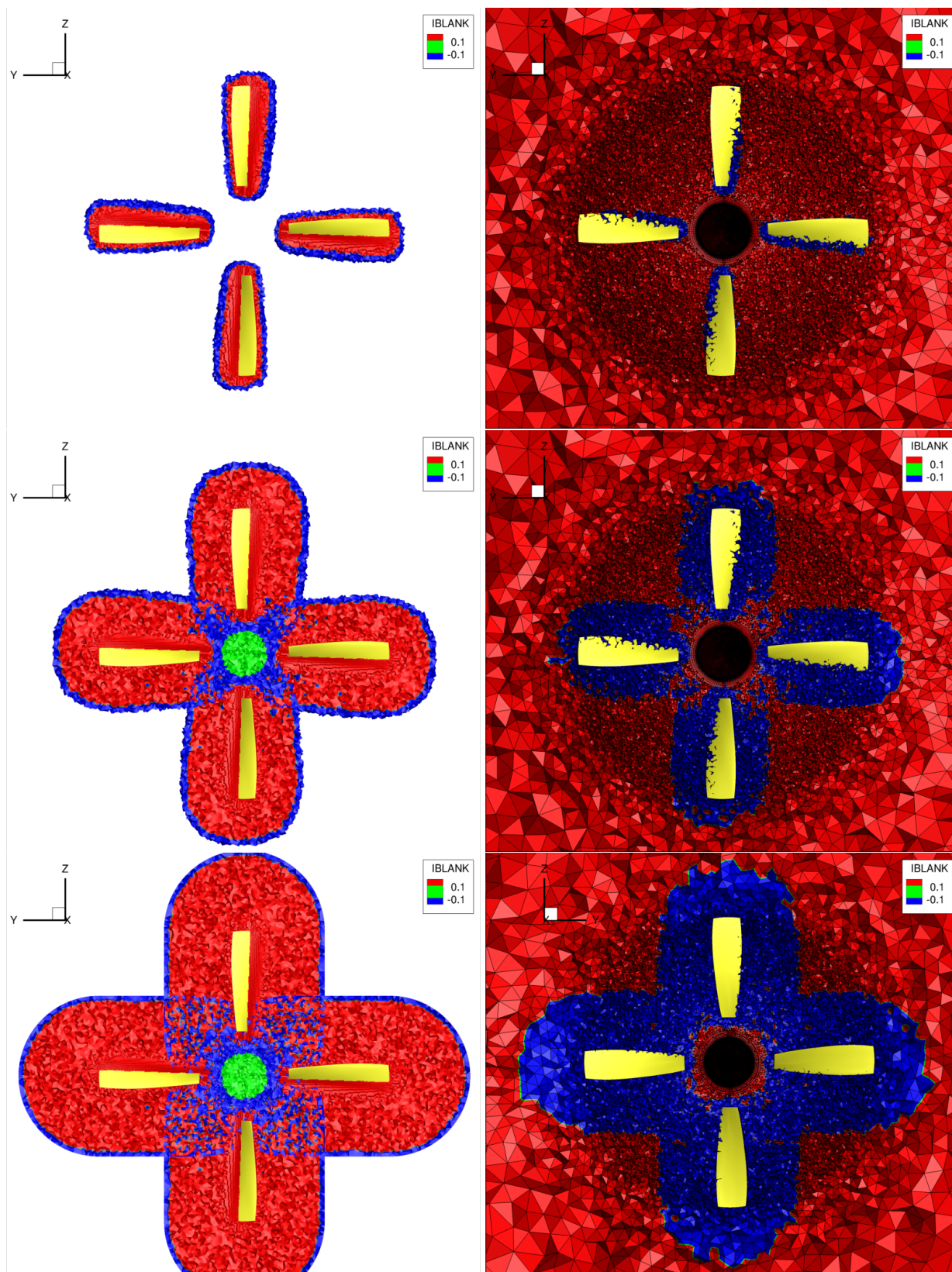
Figure 8: Mesh slices at $x = -1.45$ for overset meshes Close-Cut (top), Cut-2.5 (middle) and No-Cut (bottom).

American Institute of Aeronautics and Astronautics
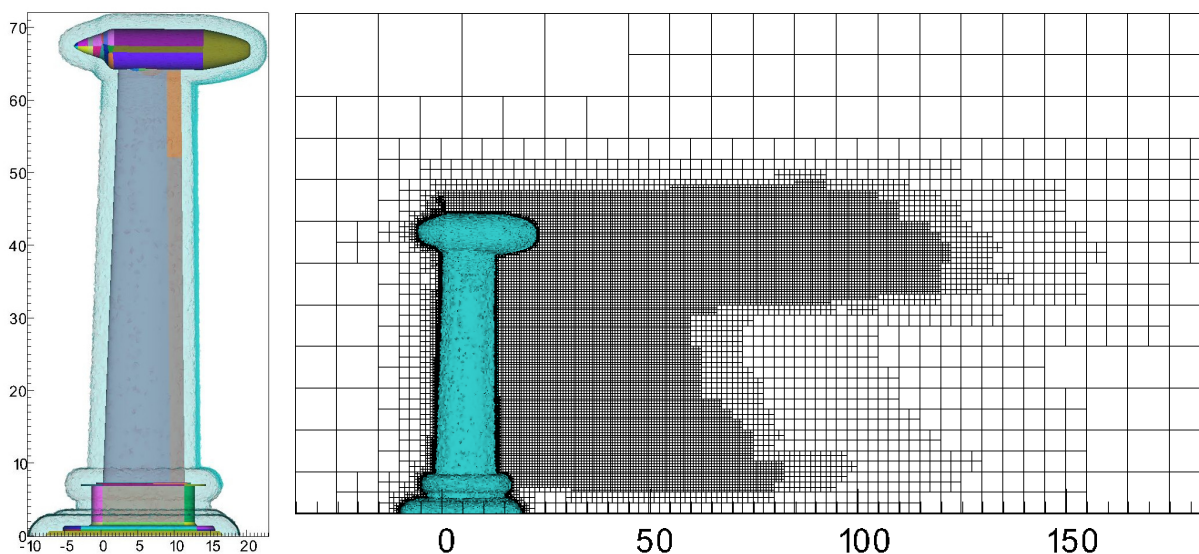
Figure 9: Near-body unstructured mesh cut to 2.0 [in] from the body surface (left) and the dynamically adapting off-body Cartesian mesh (right) used in the high-fidelity model.

the latter produces consistently higher drag values, more in agreement with experiment, although the predicted C_L values are similar between both approaches. For the blade resolved methods, the mid-fidelity and high-fidelity approaches produce results that fall closer to the experimental values throughout the range of flow incidences, with the high-fidelity hybrid RANS-LES method showing the most consistent agreement with experiment.
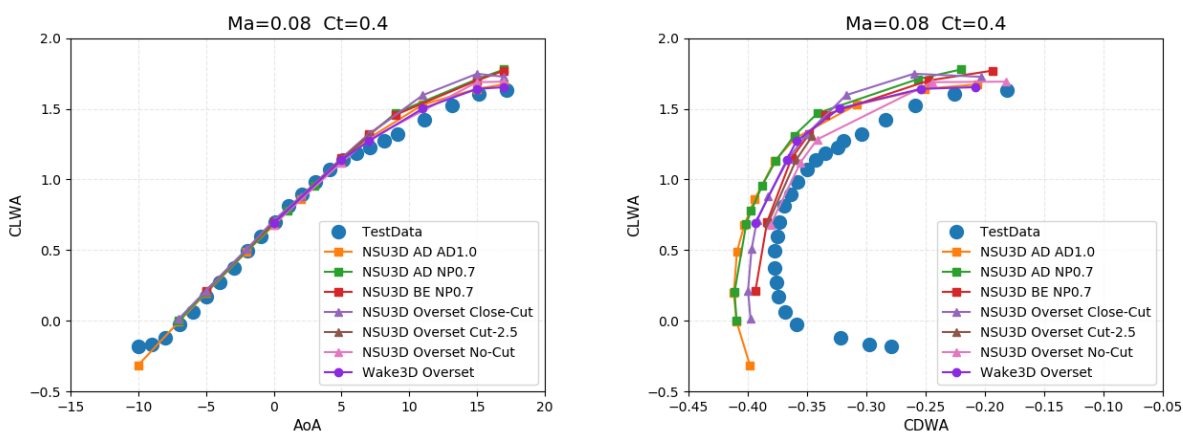
Figure 10: Comparison of lift prediction (left) and drag polars (right) with thrust included for case RUN180.
Low-Fidelity: NSU3D AD AD1.0, NSU3D AD NP0.7, NSU3D BE NP0.7
Mid-Fidelity: NSU3D Overset `Close-Cut`, NSU3D overset `Cut-2.5`, NSU3D Overset `No-Cut`
High-Fidelity: Wake3D Overset.
Key: AD-Actuator Disk with user input loading, BE-Actuator Disk with Blade-Element loading

In order to examine these results in more detail, the surface pressures on the wing computed by all methods for all flow incidences are compared in Figures 12 through 16. In general, the numerical results match the experimentally measured pressure coefficients on the wing closely at the lower angles of attack, while discrepancies appear towards $15°$ and $17°$ flow incidences, particularly at span locations closer to the propeller wake. Here again, the actuator disk results using the AD1.0 mesh agree better with experimental values at $17°$ angle of attack compared to the results obtained on the NP0.7 mesh, although some discrepancies are observed at lower angles of attack. In general, the two actuator disk methods using the NP0.7 mesh (i.e. prescribed loading and blade-element loading) agree very closely

American Institute of Aeronautics and Astronautics

with each other throughout the range of angles of attack. For the mid-fidelity overset RANS results, the no-cut blade mesh (i.e. the blade mesh which extends the furthest away from the blade) is seen to perform poorly, with premature separation occurring at 15° and 17°. In general, the best mid-fidelity results were obtained overall with the close-cut blade mesh. In general, the high-fidelity overset mesh hybrid RANS-LES simulations produce the best agreement with experimental data particularly at 15° and 17°. However, initial results obtained at these conditions using a 0.5 degree blade rotation time step performed well at low angles of attack but showed premature separation at 15° and 17°. Decreasing the time step size to 0.25 degrees resulted in the superior agreement shown in Figures 12 through 16.

The overall comparison must also take into account the convergence behavior of the various methods. The low-fidelity actuator disk model simulations use 5000 4-level non-linear multigrid cycles, taking approximately 1.6 wall-clock hours on 720 cores, totalling 1140 core-hours. Figure 17 illustrates the convergence of the actuator disk runs on the NP0.7 mesh. In general, residuals converged to low levels and the force coefficients achieved stationary values in several thousand cycles. However, for the highest flow incidence of 17°, the force coefficients did not achieve entirely stationary values, as can be seen from the figure. The mid-fidelity simulation using unsteady RANS with overset blade meshes employs a BDF2 time stepping scheme with a time step corresponding to 0.5 degrees blade rotation. Within each time step, 25 4-level multigrid sub-iterations are used. For a typical case, 8 revolutions takes about 18 to 20 wall-clock hours on 1728 cores, totalling approximately 31,104 core-hours. Figure 17 illustrates the time history of the computed force coefficients for the mid-fidelity runs, where the expected 4-per-rev periodic behavior is observed. As can be seen, the force coefficients for the lower angle of attack cases converge relatively well over 8 revolutions. However, even though the 15° and 17° cases were run out to 12 revolutions, longer time histories may be required to ensure full convergence, although these were not attempted due to resource limitations. Lastly, the high-fidelity simulations using the unsteady hybrid RANS-LES approach employed a BDF2 time-stepping scheme for the near-body RANS solver, and an explicit RK3 time-stepping scheme for the off-body LES solver. A near-body time step of 0.25 degrees blade rotation was employed for the results shown in this paper, which corresponds to the synchronization time step after which the blade meshes are rotated, the overlap communication is recomputed, and the off-body mesh is adaptively refined. For 8 rotor revolutions with dynamic wake mesh adaption, approximately 35 wall-clock hours is required running on 4608 cores, thus totalling 161,280 core-hours. The LES off-body region was initialized with 45 million degrees of freedom and grew to 350 million degrees of freedom via feature-driver mesh adaption. Figure 19 compares the history of the computed force coefficients for the 11° case between the high-fidelity RANS-LES approach and the overset RANS method. In general the high-fidelity simulations converged similarly to the mid-fidelity simulations at the lower angles of attack. At higher angles of attack, restarts from runs using larger time steps were used to accelerate the computational process for the high-fidelity runs, making a direct comparison of convergence between the two methods less meaningful.

B. Run 79 Results: Wake Survey

In this section, computed wake velocity profiles are compared with experimental data denoted as RUN79, which consists of the flow conditions: Mach=0.08, Incidence=0°, $C_T = 0.4$. Here again, the actuator disk results correspond to steady-state values obtained at the end of the convergence of the RANS equations, while the mid-fidelity overset RANS blade resolved results are obtained using averaged temporal data over one-quarter propeller revolution, and the high-fidelity RANS results employ averaging over 1.5 propeller revolutions. Figure 20 shows the axial velocity (u/U_∞) contours of the low-fidelity and mid-fidelity model runs at $Z = 0$ for RUN79, while Figure 21 shows the radial velocity (v/U_∞) contours at $Z = 0$ and Figure 22 shows the swirl velocity (w/U_∞) contours at $Z = 0$ for the same runs. For all cases, the actuator disk model is run on two meshes and the mid-fidelity model employs all three versions of the blade grid. While the contour plots show qualitatively similar behavior, more quantitative details can be seen in the line plots taken at the streamwise station $x = 1.5$ in the lower right corner of each composite figure. In the axial velocity comparisons in Figure 20, the actuator disk results on the AD1.0 mesh show higher wake velocities than those obtained on the NP0.7 mesh, which may be due to the additional refinement near the disk in the former mesh. On the same mesh (NP0.7), the prescribed loading actuator disk results overpredict the axial wake velocity, while the blade-element loading actuator disk results fall closer to the experimental data. The close-cut blade mesh in the mid-fidelity overset RANS run appears to overpredict the wake velocity as well, while the blade meshes with larger extents produce lower wake axial velocities. Overall, the high fidelity RANS-LES results produce the closest agreement with experimental data, both in terms of magnitude and profile shape. However, all numerical results show the transition from freestream to high wake velocities occurring slightly lower (in terms of r/R) than the experimental results. Additionally, a velocity deficit occurs in the region near $r/R \sim 1$, although this deficit is less pronounced in the high-fidelity results. Similar discrepancies between computational and experimental data for the wake axial velocities have been reported in previous work.[25–27]

American Institute of Aeronautics and Astronautics

From Figure 21, the radial wake velocities of all the numerical methods are seen to be in relatively close agreement with each other and with experimental data, although slight over-prediction of the experimental radial velocities is observed in the region $0.6 < r/R < 0.8$.

In Figure 22, significant differences are seen in the swirl velocities computed by the various methods. Here, the swirl velocities computed by the actuator disk with prescribed loading computed on both meshes are over-predicted, with the NP0.7 producing higher peak velocities. However, using the blade-element loading actuator disk on the same mesh (NP0.7) results in close agreement with experimental swirl velocities. For the mid-fidelity runs, the close-cut blade mesh over-predicts peak swirl velocities, while the other blade meshes predict progressively lower swirl velocities, with the no-cut mesh underpredicting swirl velocities compared to experimental values. Overall, the swirl velocities computed by the high-fidelity method and the actuator disk with blade-element loading agree best with experimental data both in terms of magnitude and profile shape.

Figure 23 compares results obtained with the two actuator disk loading models, run on the same mesh (NP0.7) to the high-fidelity model wake profiles at several downstream locations. Similar to the $x = 1.5$ location, all models suffer from early axial velocity departure towards the outboard region of the propeller for all downstream profiles. Additionally, the actuator disk methods predict a velocity deficit downstream of the propeller tip region that is not present in the experimental results, while this phenomena is much less pronounced for the high-fidelity results. The prescribed loading actuator disk results tend to overpredict the axial wake velocities, while the blade-element loading actuator disk results and the high-fidelity results show relatively good agreement with the experimental results, apart from the discrepancies in the tip region just below $r/R \sim 1$. For the radial velocities, the first three stations show overprediction of these velocity components compared to experimental values throughout the region $r/R < 1$, although the high-fidelity results compare favorably with experimental results at the most downstream station.

Moving on to the swirl velocities, the prescribed loading actuator disk results overpredict the swirl velocities at all downstream stations. The blade-element loading actuator disk results show reasonably good agreement with experimental values at the first downstream station, but tend to overpredict swirl velocities at further downstream stations. The high-fidelity results show slight under-prediction of the swirl velocities at the first two stations. However this method produces the best agreement with experimental values at the most downstream stations. Additionally, we note that the high-fidelity model is able to accurately track wakes significant distances downstream due to the use of high-order accurate discretizations and adaptive mesh refinement in the wake region, as illustrated in Figure 11.
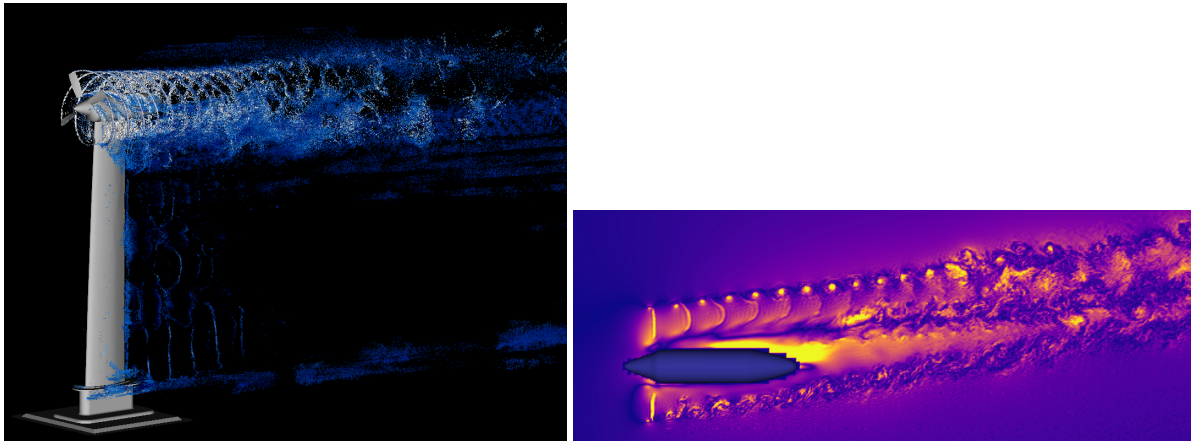

Figure 11: (left) Isosurfaces of Q-criterion at $0°$ angle of attack and (right) Instantaneous absolute swirl velocity for the high-fidelity approach using the hybrid RANS-LES model at $15°$ angle of attack.

C. Conclusions

The results presented in this paper show that the steady-state actuator-disk simulations are generally in good agreement with the overset time-dependent blade-resolved simulations for this test case, both in terms of pressure profiles on the wing and predicted wake velocities. Agreement with experimental data is also generally good, although some discrepancies are noted at high angles of attack and at the edges of the wake region. The ability of the actuator-disk approach to predict flow details such as near-wake velocity profiles is noteworthy, particularly in light of the low cost of these methods. On the one hand, it may not be surprising that an actuator disk loading obtained by

experimentally surveying the wake is capable of reproducing these same wake velocity profiles. However, the fact that the blade-element actuator disk loading shows equal or better prediction ability in this work is encouraging, since in practice the blade geometry is most often what is available to the practitioner for analysis. The actuator disk results confirm that suitable accuracy can be obtained using unstructured meshes which do not include a conforming disk surface in the mesh. However, the results indicate that actuator disk results are affected by local resolution in the disk region, although a rigorous mesh resolution study was not attempted, given the availability and use of only two meshes with dissimilar resolutions in the disk and wake regions.

For the blade-resolved simulations, the effect of the extent of the overset blade meshes was investigated for the mid-fidelity (overset unsteady-RANS) model, with the `Close-Cut` blade meshes generally showing better agreement with experimental results. Overall, the high-fidelity hybrid RANS-LES model produced better agreement with experimental data for the wing loads throughout the drag polar, as well as for the wake survey particularly at the further downstream stations.

However, these results must be seen in light of the computational cost of the different modeling approaches. The overall computational cost of the mid-fidelity blade-resolved simulations is approximately thirty times (30x) more than that required for the actuator disk simulations. The high-fidelity simulations with adaptive mesh resolution of the wake region cost approximately five times (5x) more than the mid-fidelity model. These cost comparisons are necessarily approximate, as optimizations and tuning have not been explored for reducing the cost of the blade-resolved simulations. However, for the high angle of attack cases in this work, significantly longer run times may be required to ascertain that the time-dependent results are fully statistically converged.

Although the current results have identified trends in predictive ability of the various considered methods, further studies are warranted to establish guidelines for spatial and temporal resolution as well as the effect of blade geometry modifications on overall simulation results.

D. Acknowledgements

American Institute of Aeronautics and Astronautics

References

[1]Hooker, J. R., Ginn, A. W. S. R., Walker, J., and Schiltgen, B. T., "Overview of Low Speed Wind Tunnel Testing Conducted on a Wingtip Mounted Propeller for the Workshop for Integrated Propeller Prediction," AIAA Paper 2020-2673, AIAA Aviation Forum, Virtual Event, June 2020, https://doi.org/10.2514/6.2020-2673.

[2]Ginn, S., Schiltgen, B., Hooker, R., and Wick, A., "Workshop for Integrated Propeller Prediction (WIPP) - Overview," WIPP Workshop Presentation, June 2019.

[3]Mavriplis, D. J. and Mani, K., "Unstructured Mesh Solution Techniques using the NSU3D Solver," Jan. 2014, AIAA Paper 2014-081, 52nd Aerospace Sciences Meeting, National Harbor, MD.

[4]Allmaras, S. R., Johnson, F. T., and Spalart, P. R., "Modifications and Clarifications for the Implementation of the Spalart-Allmaras Turbulence Model," 2012, ICCFD7-1902, 7th International Conference on Computational Fluid Dynamics, Big Island, Hawaii, 9-13 July.

[5]Mavriplis, D. J. and Venkatakrishnan, V., "A unified multigrid solver for the Navier-Stokes equations on mixed element meshes," *International Journal of Computational Fluid Dynamics*, , No. 8, 1997, pp. 247–263.

[6]Mavriplis, D. J., Long, M., Lake, T., and Langlois, M., "NSU3D Results for the Second AIAA High-Lift Prediction Workshop," 2014, AIAA Paper 2014-748 52nd Aerospace Sciences Meeting, National Harbor, MD.

[7]Park, M., Laflin, K. R., Chaffin, M., Powell, N., and Levy, D. W., "CFL3D, FUN3D and NSU3D contributions to the fifth drag prediction workshop," Jan. 2013, AIAA Paper 2013-0050, 51st AIAA Aerospace Sciences Meeting, Grapevine TX.

[8]Brazell, M. J., Kirby, A. C., Sitaraman, J., and Mavriplis, D. J., "A multi-solver overset mesh Approach for 3D mixed element variable order discretizations," AIAA Paper 2016-2053, 54th AIAA Aerospace Sciences Meeting, San Diego, CA., June 2016.

[9]Brazell, M. J., Kirby, A. C., and Mavriplis, D. J., "A high-order discontinuous-Galerkin octree-based AMR solver for overset simulations," AIAA Paper 2017-3944, 23rd AIAA Computational Fluid Dynamics Conference, Denver, CO., June 2017.

[10]Kirby, A. C., *Enabling high-order methods for extreme-scale simulations*, University of Wyoming, 2018.

[11]Brazell, M. J., Brazell, M. J., Stoellinger, M. K., Mavriplis, D. J., and Kirby, A. C., "Using LES in a Discontinuous Galerkin method with constant and dynamic SGS models," AIAA Paper 2015-0060, 53rd AIAA Aerospace Sciences Meeting, Kissimmee, FL., January 2015.

[12]Kirby, A. C., Mavriplis, D. J., and Wissink, A. M., "An Adaptive Explicit 3D Discontinuous Galerkin Solver for Unsteady Problems," AIAA Paper 2015-3046, 22nd AIAA Computational Fluid Dynamics Conference, Dallas, TX, June 2015.

[13]Burstedde, C., Wilcox, L. C., and Ghattas, O., "p4est: Scalable algorithms for parallel adaptive mesh refinement on forests of octrees," *SIAM Journal on Scientific Computing*, Vol. 33, No. 3, 2011, pp. 1103–1133.

[14]Smagorinsky, J., "General circulation experiments with the primitive equations: I. The basic experiment," *Monthly weather review*, Vol. 91, No. 3, 1963, pp. 99–164.

[15]Gassner, G. J., Winters, A. R., and Kopriva, D. A., "Split form nodal discontinuous Galerkin schemes with summation-by-parts property for the compressible Euler equations," *Journal of Computational Physics*, Vol. 327, 2016, pp. 39–66.

[16]Kirby, A. C., Brazell, M. J., Yang, Z., Roy, R., Ahrabi, B. R., Stoellinger, M. K., Sitaraman, J., and Mavriplis, D. J., "Wind farm simulations using an overset hp-adaptive approach with blade-resolved turbine models," *The International Journal of High Performance Computing Applications*, Vol. 33, No. 5, 2019, pp. 897–923.

[17]Edmonds, A. P., Hassanzadeh, A., Kirby, A. C., Mavriplis, D. J., and Naughton, J. W., "Effects of Blade Load Distributions on Wind Turbine Wake Evolution Using Blade-Resolved Computational Fluid Dynamics Simulations," AIAA Paper 2019-2081, 57th AIAA Aerospace Sciences Meeting, San Diego, CA., January 2019.

[18]Kirby, A. C., Hassanzadeh, A., Mavriplis, D. J., and Naughton, J. W., "Wind turbine wake dynamics analysis using a high-fidelity simulation framework with blade-resolved turbine models," AIAA Paper 2018-0256, AIAA SciTech Wind Energy Symposium, Kissimmee, FL., January 2018.

[19]Kara, K., Brazell, M. J., Kirby, A. C., Mavriplis, D. J., and Duque, E. P., "Hover predictions using a high-order discontinuous galerkin off-body discretization," AIAA Paper 2020-0771, AIAA Scitech 2020 Forum, Orlando, FL., January 2020.

[20]David M. O'Brien, J., *Analysis Of Computational Modeling Techniques For Complete Rotorcraft Configurations*, Ph.D. thesis, Georgia Institute of Technology, 2006.

[21]Nygaard, T. A., Dimanlig, A. C., and Meadowcroft, E. T., "Application of a Momentum Source Model to the RAH-66 Comanche FANTAIL," American Helicopter Society 4th Decennial Specialist's Conference on Aeromechanics, San Francisco, CA, Jan 2004.

[22]Valarezo, W. and Mavriplis, D., "Navier-Stokes Applications to High-Lift Airfoils," *Journal of Aircraft*, Vol. 32, No. 3, 1995, https://doi.org/10.2514/3.46764.

[23]Roget, B. and Sitaraman, J., "Robust and efficient overset grid assembly for partitioned unstructured meshes," *Journal of Computational Physics*, Vol. 260, 2014, pp. 1–24.

[24]Brazell, M. J., Sitaraman, J., and Mavriplis, D. J., "An overset mesh approach for 3D mixed element high-order discretizations," *Journal of Computational Physics*, Vol. 322, 2016, pp. 33–51.

[25]Reveles, N. D., Seledic, K., Williams, D., Blades, E. L., and Shah, P., "Rotor/Propeller Model Fidelity Effects on Propeller-Wing Interactional Aerodynamics," AIAA Paper 2020-2676, AIAA Aviation Forum, Virtual Event, June 2020, https://doi.org/10.2514/6.2020-2676.

[26]Crawford, A. M. and Sreenivas, K., "Helios and Tenasi Results for the Workshop for Integrated Propeller Prediction," AIAA Paper 2020-2675, AIAA Aviation Forum, Virtual Event, June 2020, https://doi.org/10.2514/6.2020-2675.

[27]Aref, P., Ghoreyshiy, M., Hummer, C. J., Jirasek, A., and Seidel, J., "Application of the HPCMP CREATE-AV Kestrel to the 1st AIAA Workshop for Integrated Propeller Prediction," AIAA Paper 2020-2674, AIAA Aviation Forum, Virtual Event, June 2020, https://doi.org/10.2514/6.2020-2674.

American Institute of Aeronautics and Astronautics
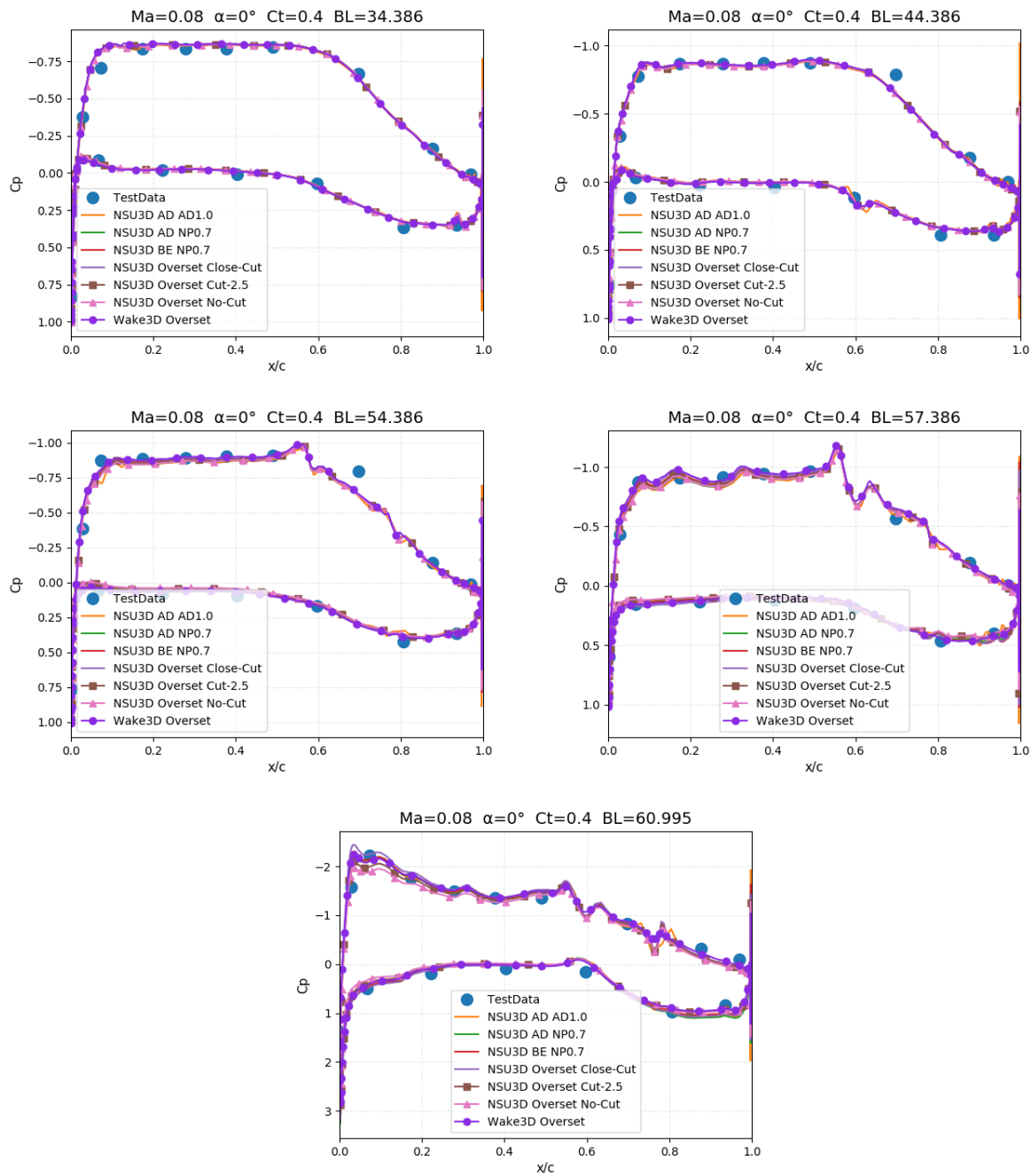
Figure 12: Comparison of computed surface pressures using various fidelity models with experimental data for RUN180 at $\alpha = 0°$.

American Institute of Aeronautics and Astronautics
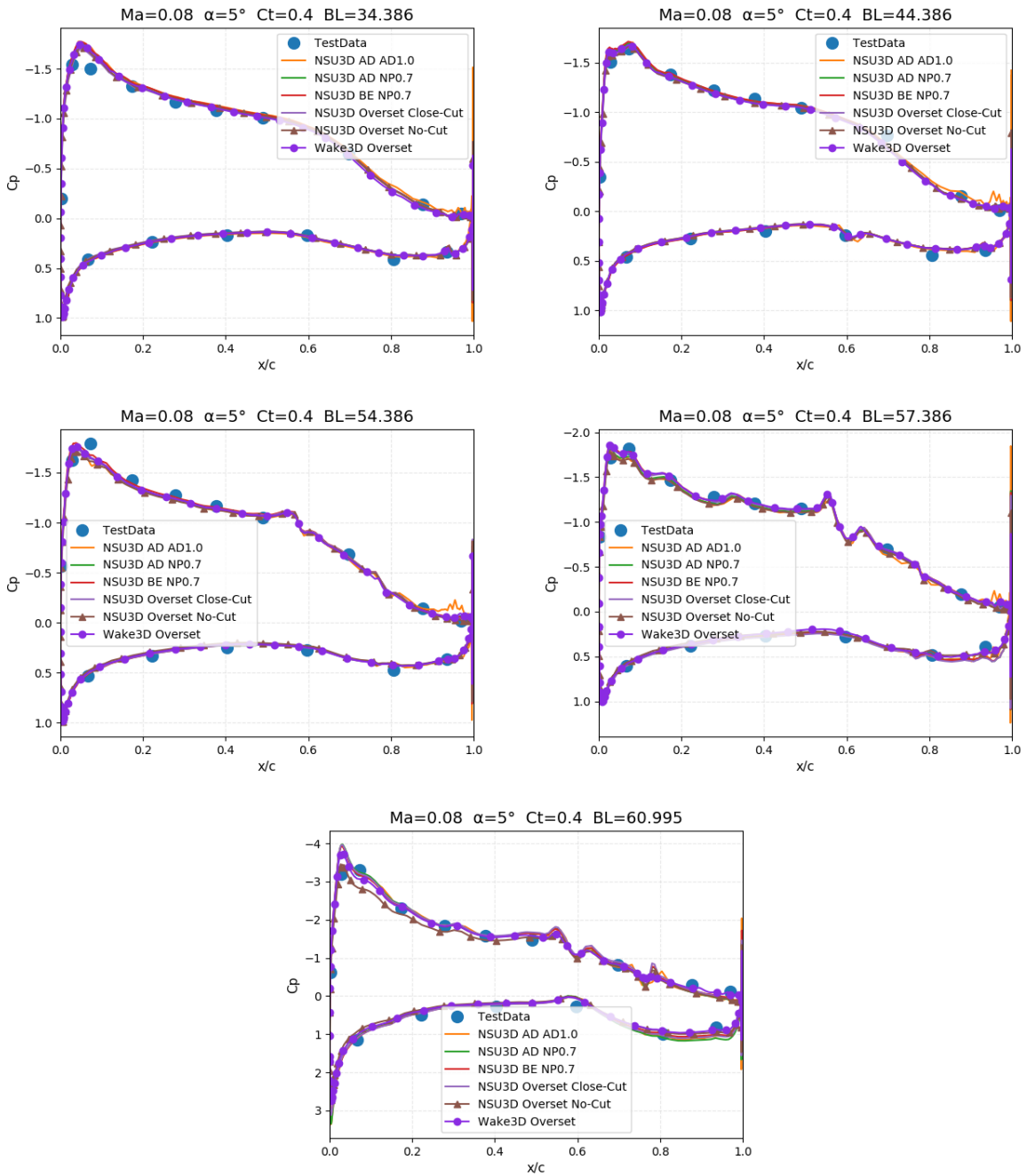
Figure 13: Comparison of computed surface pressures using various fidelity models with experimental data for RUN180 at $\alpha = 5°$.
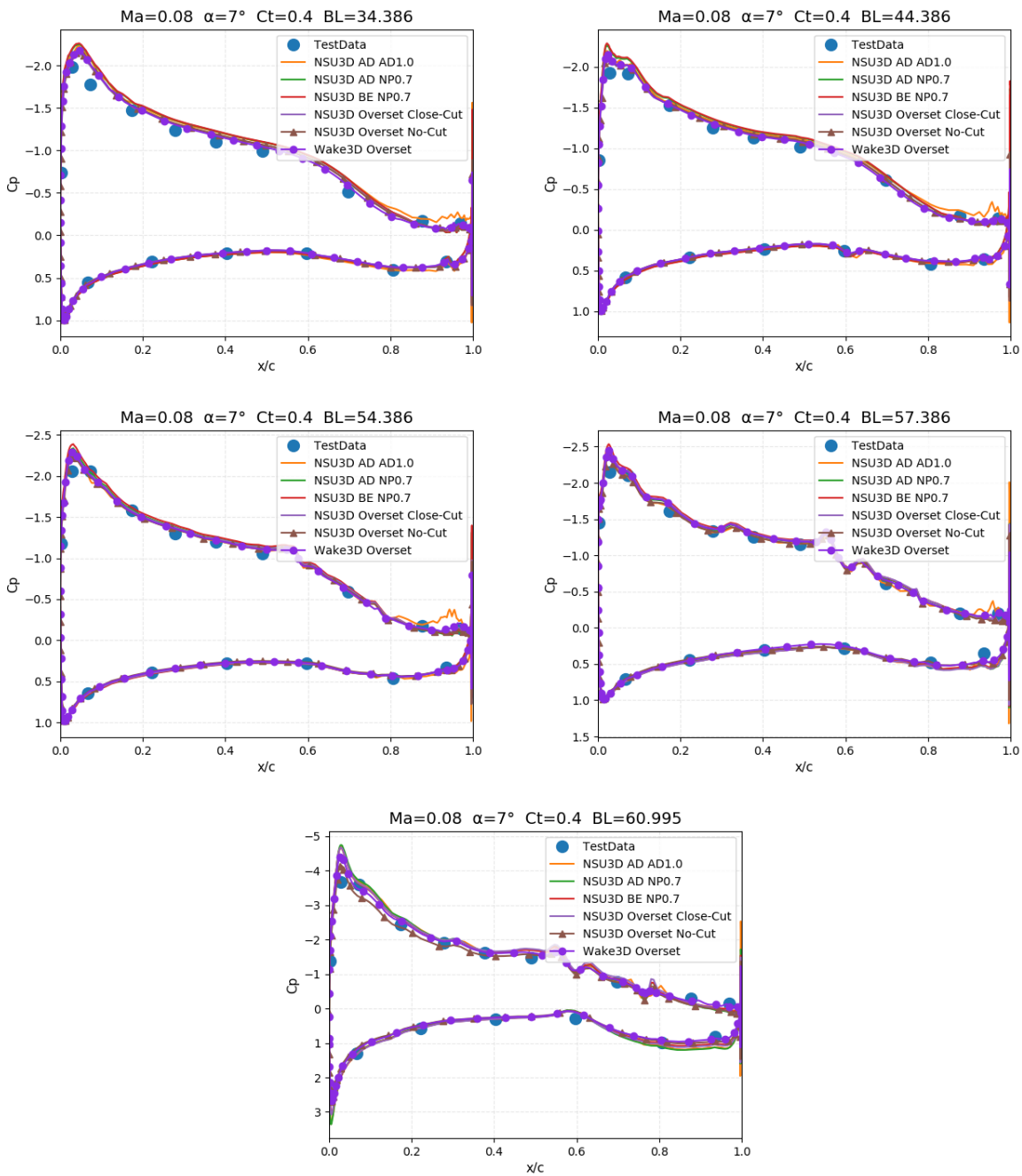
Figure 14: Comparison of computed surface pressures using various fidelity models with experimental data for RUN180 at $\alpha = 7°$.
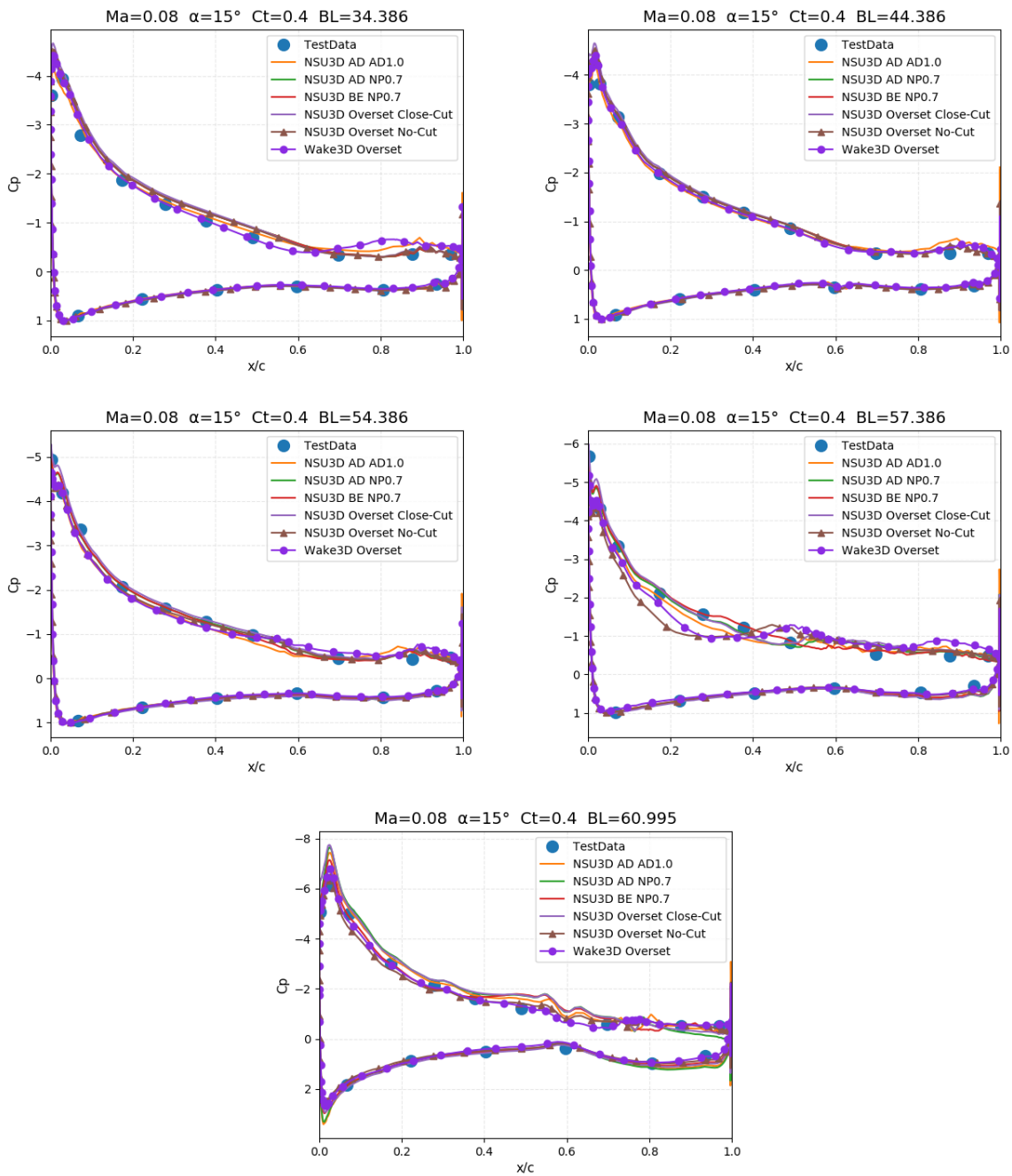
Figure 15: Comparison of computed surface pressures using various fidelity models with experimental data for RUN180 at $\alpha = 15°$.
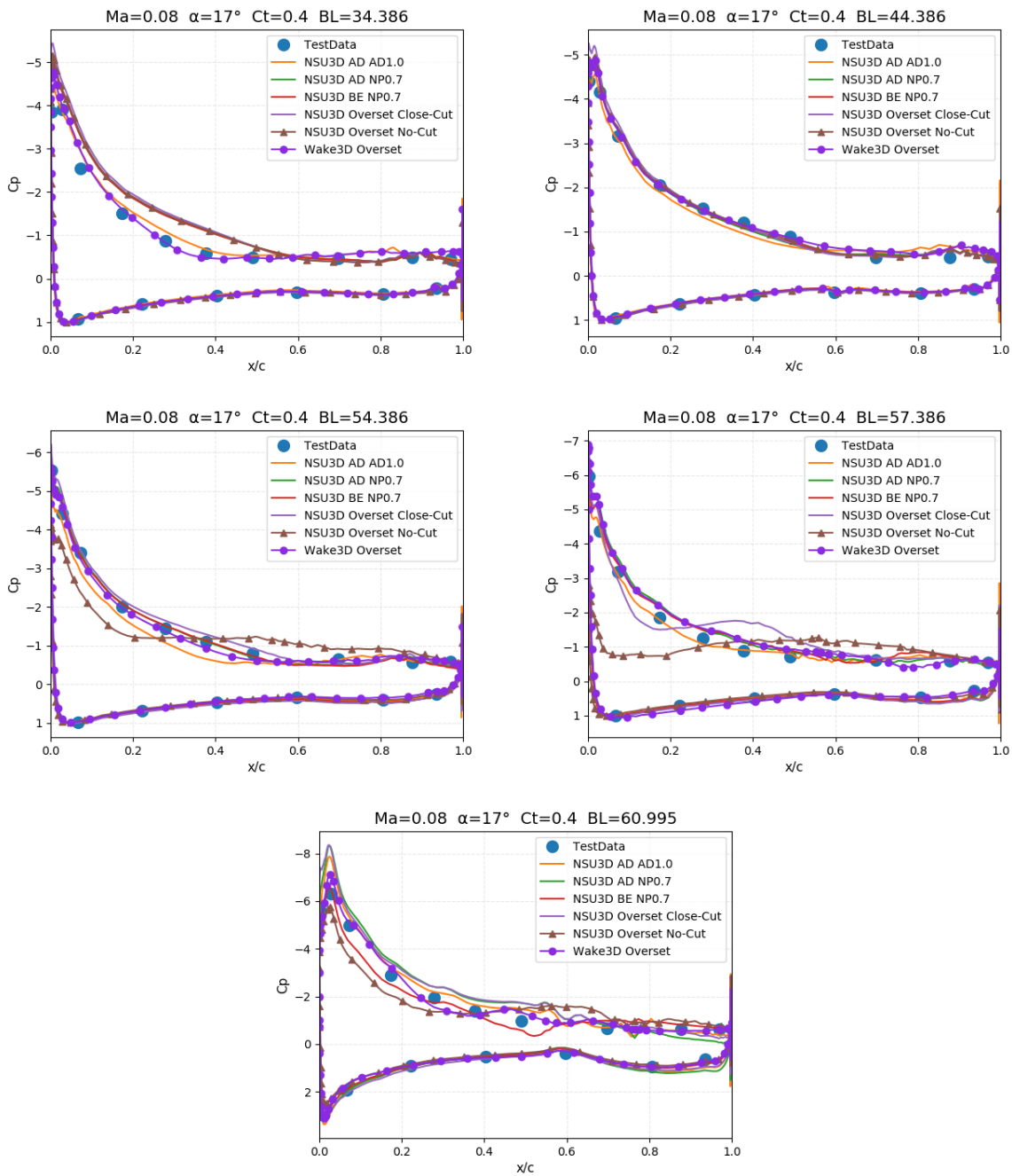
Figure 16: Comparison of computed surface pressures using various fidelity models with experimental data for RUN180 at $\alpha = 17°$.

American Institute of Aeronautics and Astronautics
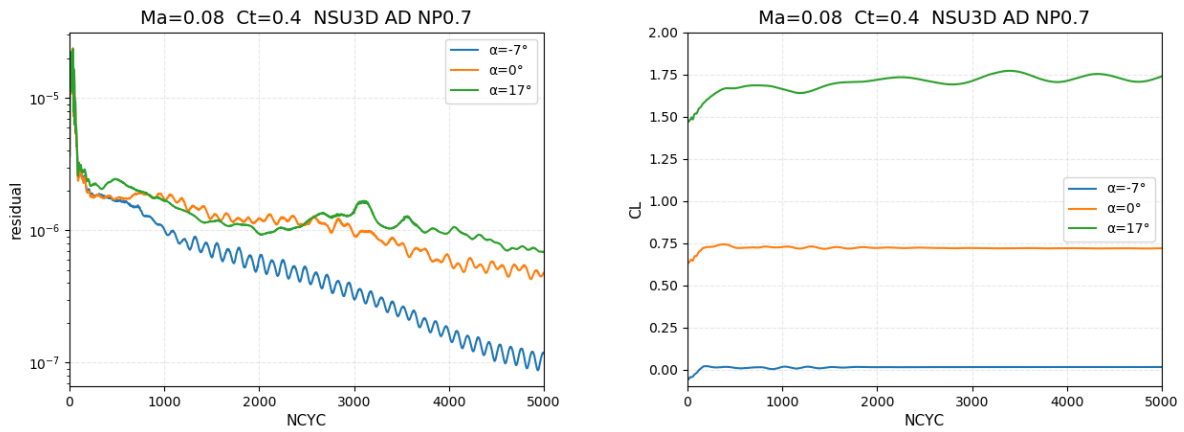
Figure 17: Steady-state residual convergence history (left) and lift coefficient convergence history (right) for actuator disk runs on mesh NP0.7 for case RUN180.
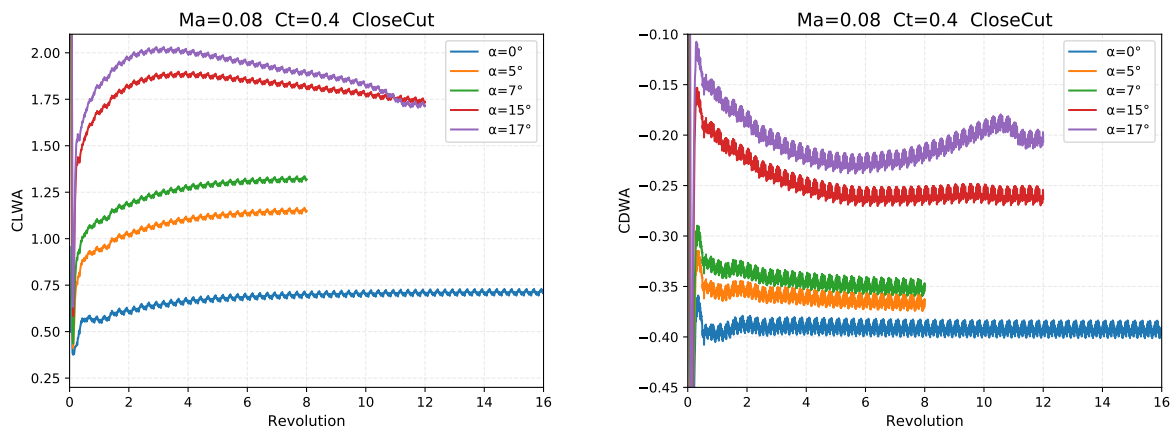

Figure 18: Comparison of lift history (left) and drag history (right) for the mid-fidelity model on the overset Close-Cut mesh, case RUN180.

American Institute of Aeronautics and Astronautics
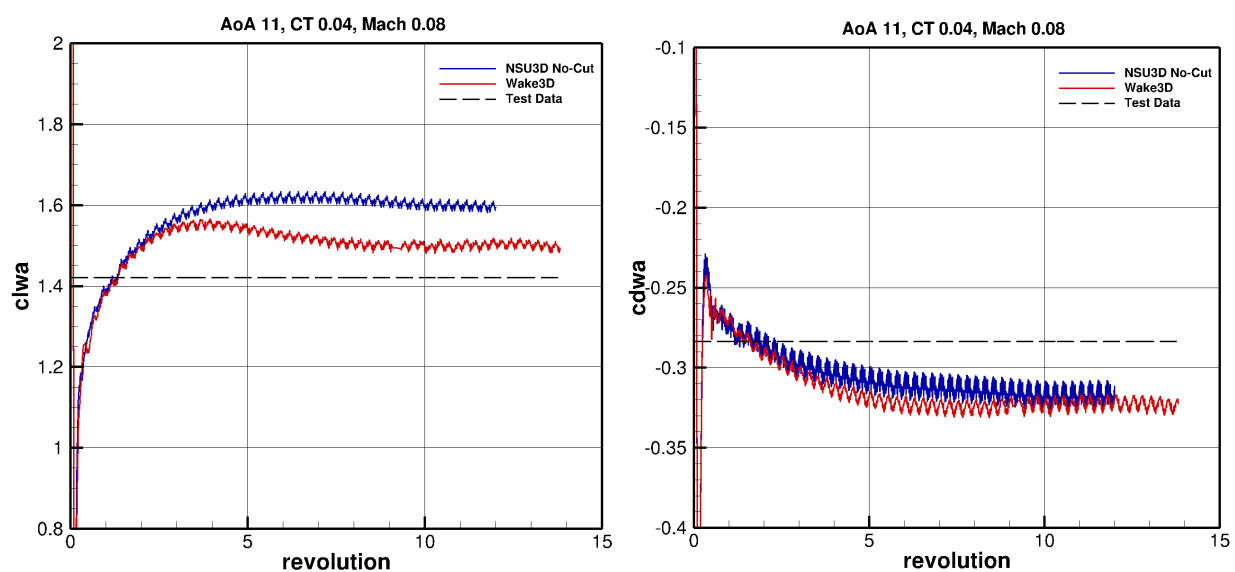
Figure 19: Comparison of lift history (left) and drag history (right) for the hybrid RANS-LES model (Wake3D) using the trimmed off-body wing-body mesh (2 [in]) and the RANS-only model (NSU3D) on the untrimmed off-body wing-body mesh, for case RUN180 at 11 degrees angle of attack.

American Institute of Aeronautics and Astronautics
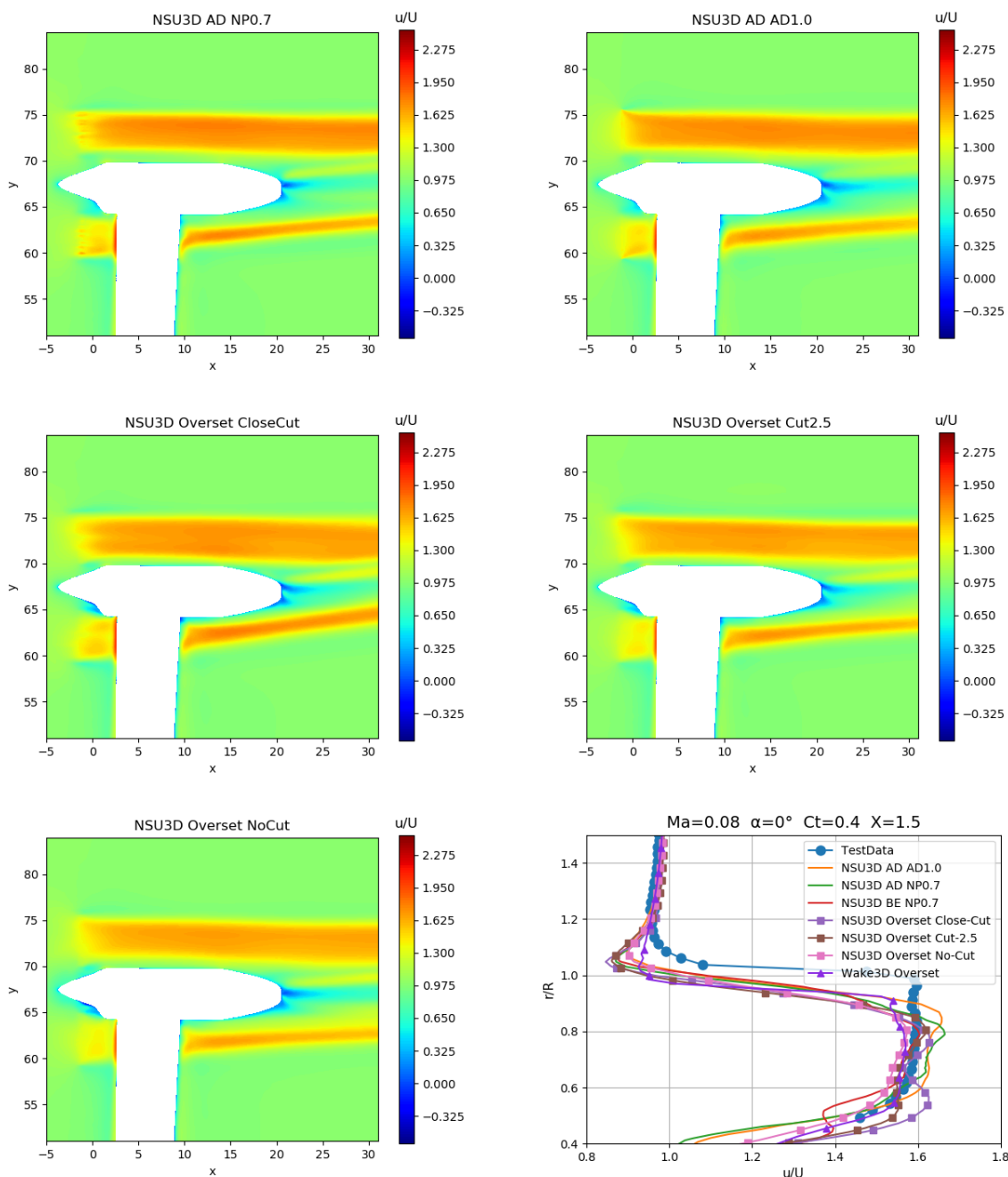
Figure 20: Axial velocity (u/U_∞) contours of NSU3D at $Z = 0$ for mesh NP0.7 (top left), mesh AD1.0 (top right), overset mesh Close-Cut (bottom left) and overset mesh No-Cut (bottom right) case RUN79 $\alpha = 0^\circ$.

American Institute of Aeronautics and Astronautics
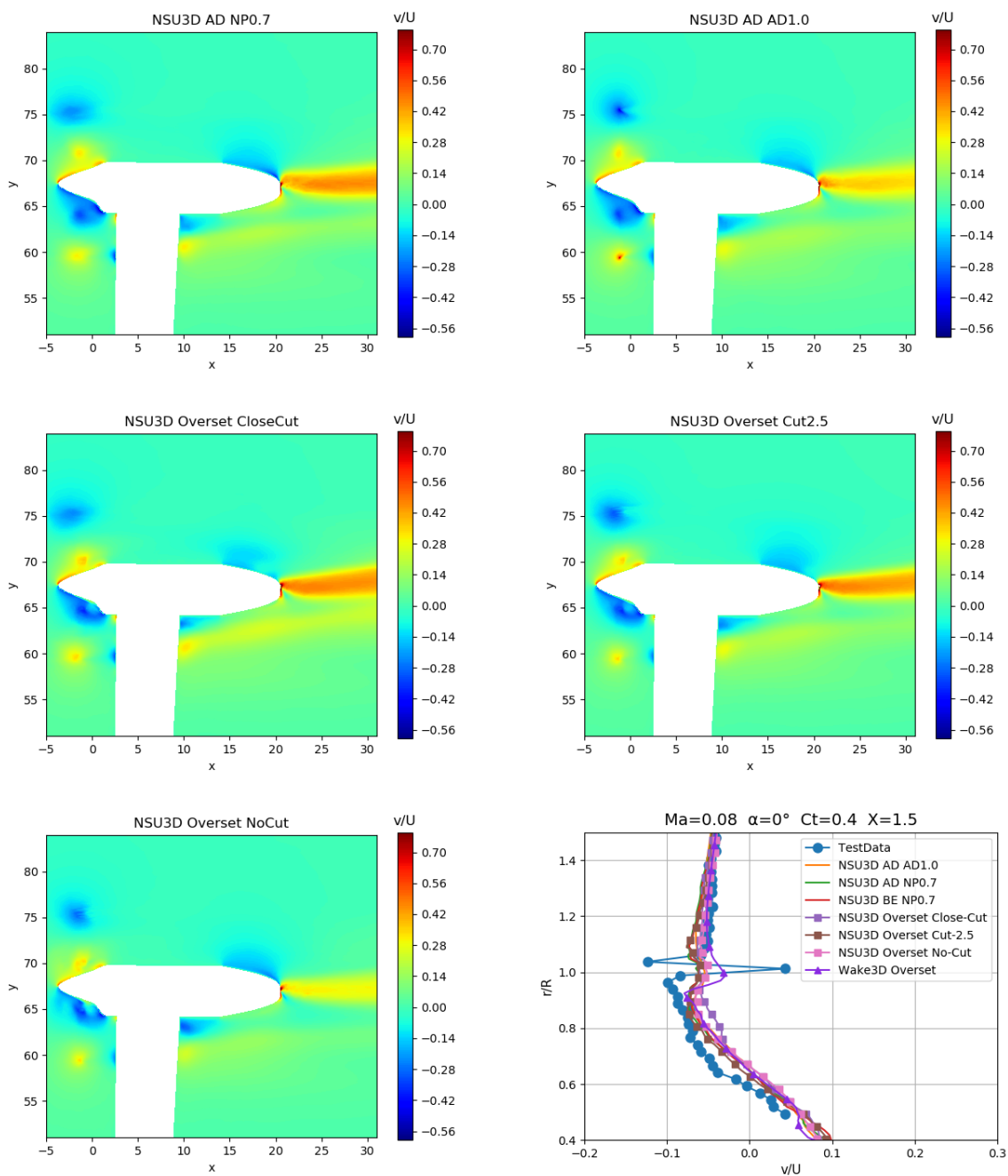
Figure 21: Radial velocity (v/U_∞) contours of NSU3D at $Z = 0$ for mesh NP0.7 (top left), mesh AD1.0 (top right), overset mesh Close-Cut (bottom left) and overset mesh No-Cut (bottom right) case RUN79 $\alpha = 0°$.

American Institute of Aeronautics and Astronautics
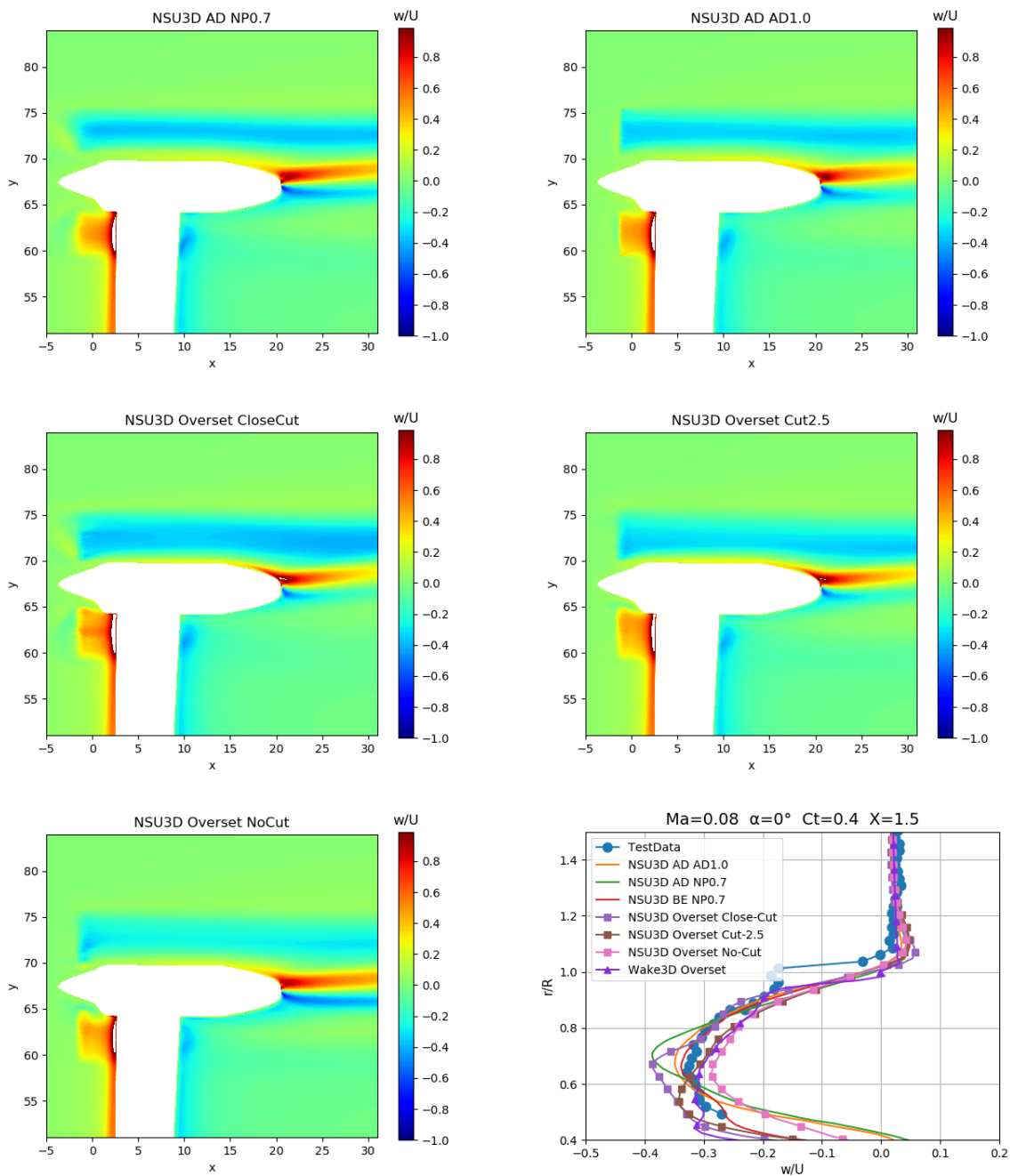
Figure 22: Swirl velocity (w/U_∞) contours of NSU3D at $Z = 0$ for mesh NP0.7 (top left), mesh AD1.0 (top right), overset mesh Close-Cut (bottom left) and overset mesh No-Cut (bottom right), case RUN79 $\alpha = 0°$.

American Institute of Aeronautics and Astronautics

Wake Profiles

Axial

Radial

Swirl
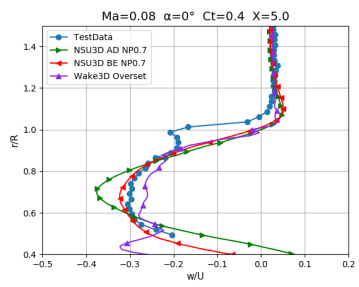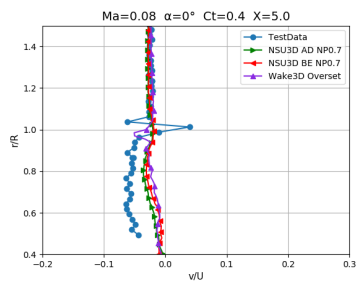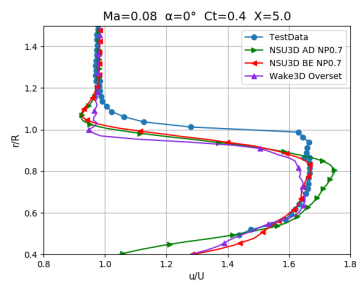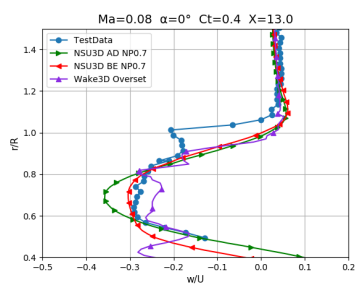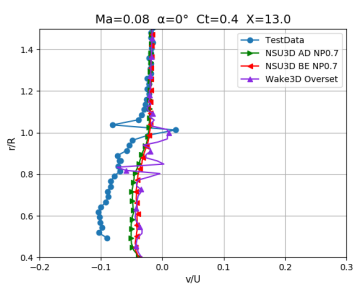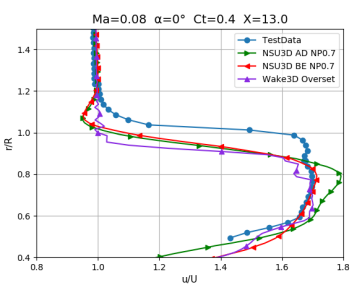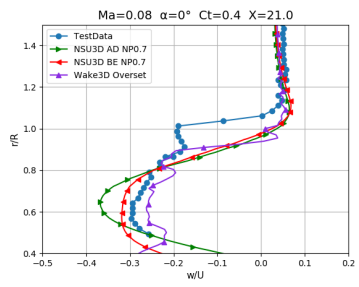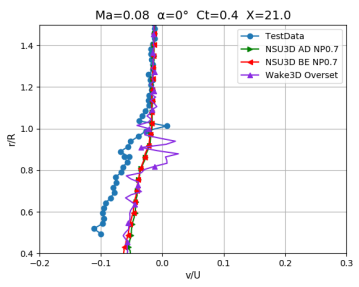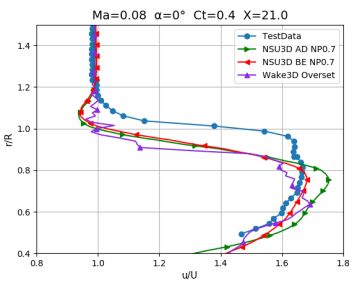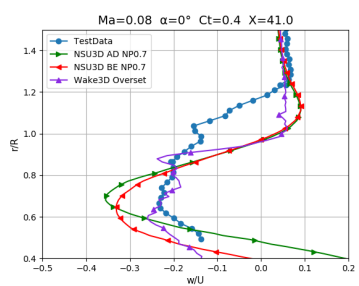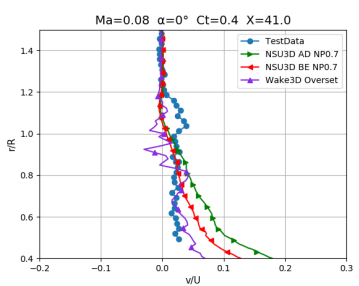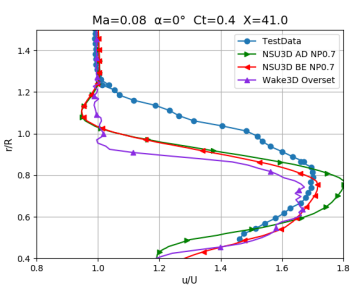
Figure 23: Axial (u/U_∞), radial (v/U_∞), and swirl (w/U_∞) velocity components at downstream wake positions for the low-fidelity actuator disk model and the high-fidelity hybrid RANS-LES model at $Ma = 0.08$, $C_t = 0.4$, 0 degrees angle of attack.

American Institute of Aeronautics and Astronautics